Monthly Notices of the ROYAL ASTRONOMICAL SOCIETY

MNRAS **546,** 1–19 (2026) https://doi.org/10.1093/mnras/stag238
Advance Access publication 2026 February 05

Extending the frontier of spatially resolved supermassive black hole mass measurements to at $1 \lesssim z \lesssim 2$: simulations with ELT/MICADO high-resolution mass models and HARMONI integral-field stellar kinematics

Dieu D. Nguyen [1]★ Michele Cappellari [2]★ Tinh Q. T. Le [3] Hai N. Ngo [4] Elena Gallo [1] Niranjan Thatte [2] Fan Zou [1] Tien H. T. Ho [4] Tuan N. Le [5] Huy G. Tong [4] and Miguel Pereira-Santaella [6]

[1]*Department of Astronomy, University of Michigan, 1085 South University Avenue, Ann Arbor, MI 48109, USA*
[2]*Sub-Department of Astrophysics, Department of Physics, University of Oxford, Denys Wilkinson Building, Keble Road, Oxford, OX1 3RH, UK*
[3]*Department of Physics, International University, Vietnam National University in Ho Chi Minh City, Vietnam*
[4]*Faculty of Physics–Engineering Physics, University of Science, Vietnam National University in Ho Chi Minh City, Vietnam*
[5]*International Centre for Interdisciplinary Science and Education, 07 Science Avenue, Ghenh Rang, 55121 Quy Nhon, Vietnam*
[6]*Instituto de Física Fundamental, CSIC, Calle Serrano 123, 28006 Madrid, Spain*

Accepted 2026 February 3. Received 2025 December 22; in original form 2025 November 7

ABSTRACT

Current spatially resolved kinematic measurements of supermassive black hole (SMBH) masses are largely confined to the local Universe (distances $\lesssim 100$ Mpc). We investigate the potential of the Extremely Large Telescope's (ELT) first-light instruments, MICADO and HARMONI, to extend these dynamical measurements to galaxies at redshift $1 \lesssim z \lesssim 2$. We select a sample of five bright, massive, quiescent galaxies at these redshifts, adopting their Sérsic profiles, from *HST* photometry, as their intrinsic surface brightness distributions. Based on these intrinsic models, we generate mock MICADO images using SimCADO and mock HARMONI integral-field spectroscopic data cubes using HSIM. The HARMONI simulations utilize input stellar kinematics derived from Jeans Anisotropic Models (JAM). We then process these mock observations: the simulated MICADO images are fitted with Multi-Gaussian Expansion (MGE) to derive stellar mass models, and stellar kinematics are extracted from mock HARMONI cubes with pPXF. Finally, these derived stellar mass models and kinematics are used to constrain JAM dynamical models within a Bayesian framework. Our analysis demonstrates that SMBH masses can be recovered with an accuracy of ∼10 per cent. We find that MICADO can provide detailed stellar mass models with ∼1 hour of on-source exposure. HARMONI requires longer minimum integrations for reliable stellar kinematic measurements of SMBHs. The required on-source time scales with apparent brightness, ranging from 5–7.5 hours for galaxies at $z \approx 1$ (F814W, 20–20.5 mag) to 5 hours for galaxies at $1 < z \lesssim 2$ (F160W, 20.8 mag). These findings highlight the ELT's capability to push the frontier of SMBH mass measurements to $z \approx 2$, enabling crucial tests of SMBH-galaxy co-evolution at the top end of the galaxies mass function.

Key words: galaxies: evolution – galaxies: formation – galaxies: general – galaxies: kinematics and dynamics – galaxies: nuclei – galaxies: supermassive black holes.

1 INTRODUCTION

1.1 SMBH-galaxy co-evolution and observational challenges

It is well established that the mass of nearby supermassive black holes (SMBHs, $M_{\rm BH} \approx 10^{6-9}$ M$_\odot$) correlates with the macroscopic properties of massive galaxies ($M_\star \gtrsim 10^{10}$ M$_\odot$; see review by J. Kormendy & L. C. Ho 2013). Notable correlations include the $M_{\rm BH}$–galaxy stellar mass ($M_\star$; J. Magorrian et al. 1998), the $M_{\rm BH}$–velocity dispersion ($\sigma_\star$) of the stars in a galaxy (L. Ferrarese & D. Merritt 2000; K. Gebhardt et al. 2000), and the $M_{\rm BH}$–luminosity (L_K; J. Kormendy & D. Richstone 1995). These correlations indicate the mutual growth of both black holes (BHs) and their host galaxies; see reviews by A. C. Fabian (2012), J. Kormendy & L. C. Ho (2013), and J. E. Greene, J. Strader & L. C. Ho (2020).

The discovery of these correlations has primarily relied on dynamical modelling of the stellar kinematics, for both massive galaxies (e.g. K. Gebhardt et al. 2003; M. Cappellari et al. 2009; N. J. McConnell et al. 2011; S. P. Rusli et al. 2013; J. L. Walsh

★ E-mail: dieun@umich.edu(DN); michele.cappellari@physics.ox.ac.uk(MC)

et al. 2016; S. Thater et al. 2022, 2023) and lower mass ones (e.g. D. D. Nguyen et al. 2014, 2017, 2018, 2019, 2025c; D. D. Nguyen 2017; C. P. Ahn et al. 2018; K. T. Voggel et al. 2018). BH determination were also performed using gas kinematics from either ionized gas (e.g. A. J. Barth et al. 2001; K. L. Shapiro et al. 2006; J. L. Walsh et al. 2013) or molecular gas (e.g. A. J. Barth et al. 2016; K. Onishi et al. 2017; D. D. Nguyen 2019; T. A. Davis et al. 2020; D. D. Nguyen et al. 2020, 2021, 2022; H. N. Ngo et al. 2025c). These direct dynamical BH determinations have so far only been accessible to within about 100 Mpc (see compilations by R. P. Saglia et al. 2016; R. C. E. den Bosch 2016). Beyond this distance, current facilities cannot resolve the SMBH's sphere of influence (SOI[1]), the region where its gravity dominates. The angular size of the BH SOI ($R_{\rm SOI}$) in galaxies is typically much smaller than 0.1 arcsec (T. Zeeuw 2001, equation 2), falling below the diffraction limit of current world-leading telescopes equipped with adaptive optics (AO), such as the Gemini Telescope, the Very Large Telescope (VLT), and the Keck Telescope, which achieve a point spread function (PSF) full width at half maximum (FWHM) of approximately 0.1 arcsec.

On the other hand, the Atacama Large Millimeter/submillimeter Array (ALMA) is now capable of achieving angular resolutions of ~ 0.01 arcsec in Band 6 observations of ^{12}CO(2−1) emission using the longest baseline antenna configuration (i.e. C−10), comparable to the spatial scales explored in the simulations presented in this work. However, such ultra-high-angular-resolution molecular gas observations often reveal resolved central cavities or deficits in the ^{12}CO(2−1) circumnuclear disc emission, likely caused by active galactic nuclei (AGNs; M. Imanishi et al. 2020; T. Izumi et al. 2020; D. D. Nguyen et al. 2021), which can degrade the accuracy of SMBH mass measurements, as demonstrated in the mm-Wave Interferometric Survey of Dark Object Masses (WISDOM; e.g. M. D. Smith et al. 2019) and the Measuring Black Holes in Below Milky Way Stellar Mass (M⋆) Galaxies (MBHBM⋆; e.g. D. D. Nguyen et al. 2020) projects. Another common limitation of using ALMA at ultra-high angular resolution to dynamically measure SMBH masses is that a significant fraction of the ^{12}CO(2–1) emission from the circumnuclear gas disc can be resolved out. This loss of large-scale flux reduces the sensitivity and hampers the recovery of robust molecular gas kinematics. In principle, this effect can be mitigated by combining multiple measurement sets obtained with different array configurations, spanning a range of angular resolutions and maximum recoverable scales (e.g. combining the longest-baseline configuration, C–10, with more compact configurations such as C–8 and C–5). However, such multiconfiguration observations are observationally expensive and typically require total on-source integration times in excess of ∼40 h to achieve sufficient sensitivity, making this approach impractical for large samples.

Estimates of high-redshift AGN and quasars suggest that their $M_{\rm BH}$ are much larger than predictions from the local galaxy stellar mass versus BH scaling relations (e.g. R. Maiolino et al. 2024). This implies that these correlations may have evolved over cosmic time. However, these BH estimates are not spatially resolved and must rely on strong assumptions and could suffer from significant measurement biases. Consequently, the evolution of the galaxy–BH scaling relation with redshift remains observationally unconstrained using direct dynamical methods, leaving open questions about how both BHs and their host galaxies grow in the context of galaxy–BH co-evolution.

[1]The spherical region surrounding a BH where its gravitational force dominates, defined as the vicinity within which the enclosed mass equals twice the $M_{\rm BH}$: this can be approximately estimated as $R_{\rm SOI} \approx GM_{\rm BH}/\sigma_\star^2$, where G represents the gravitational constant.

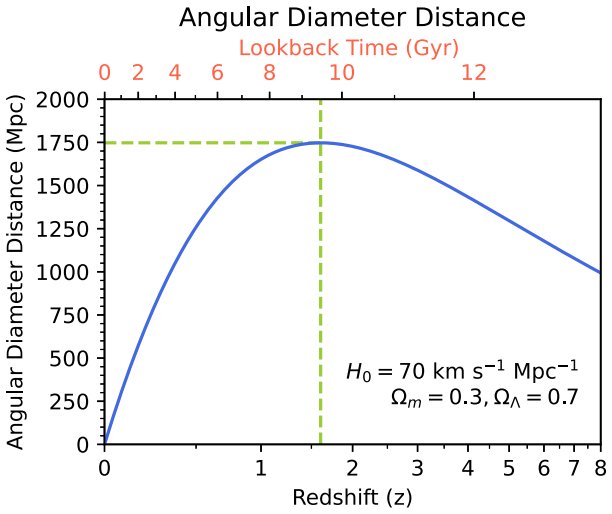

Figure 1. Angular-diameter distance ($D_{\rm A}$) versus redshift (z) in a standard flat concordance lambda cold dark matter (ΛCDM) cosmology, showing $D_{\rm A}$ peaking at ≈ 1750 Mpc around $z \approx 1.6$.

1.2 The promise of the ELT for high-redshift SMBH demographics

The advent of the Extremely Large Telescope (ELT) and its first-generation instruments – namely, the Multi-AO Imaging Camera for Deep Observations (MICADO) imager (R. Davies et al. 2010, 2021) and the High Angular Resolution Monolithic Optical and Near-infrared Integral (HARMONI) field spectrograph (N. A. Thatte et al. 2016, 2020) – promises spatial resolutions around 10 milliarcseconds (mas). This capability potentially enables direct spatially-resolved mass measurements for $\gtrsim 10^9$ M$_\odot$ SMBHs out to cosmological distances.

Dynamically weighing SMBHs requires resolving the line-of-sight (LOS) movements of stars or gas at scales corresponding to $R_{\rm SOI}$. The angular size subtended by a physical scale like $R_{\rm SOI}$ depends on the angular-diameter distance ($D_{\rm A}$). Crucially, in standard cosmological models, $D_{\rm A}(z)$ does not increase monotonically with redshift z. As shown in Fig. 1, it reaches a maximum value of $D_{\rm A} \approx 1750$ Mpc around $z \approx 1.6$ and then decreases. This means that, counterintuitively, very distant objects of a given size can appear slightly larger in angular size than objects at intermediate redshifts. For example, a galaxy with $\sigma_\star \approx 300$ km s^{-1} hosting an SMBH with $M_{\rm BH} \approx 1.8 \times 10^9$ M$_\odot$ according to the $M_{\rm BH}$–$\sigma_\star$ relation (J. Kormendy & L. C. Ho 2013, equation 3) has an $R_{\rm SOI}$ that would subtend ≈ 10 milliarcseconds (mas) at a distance $D_{\rm A} \approx 1800$ Mpc. But this distance is larger than the peak $D_{\rm A}$. This implies that this $R_{\rm SOI}$ could in principle be resolved at any redshift. This angular scale is within the reach of the ELT's resolution.

However, even if the SOI is angularly resolved, observing high-redshift objects presents a significant challenge due to cosmological surface brightness dimming, which produces a steep decrease of the observed *bolometric* surface brightness $\Sigma \propto (1+z)^{-4}$. The

Table 1. Photometric properties of simulated galaxies.

Galaxy name	α(J2000)	δ(J2000)	z	q	m (filter)	R_e	n	lg $M_\star$	σ_e	D_A	Scale
	(h:m:s)	(° ′ ″)		(b/a)	(total mag)	(arcsec)		($M_\odot$)	(km s^{-1})	(Mpc)	(kpc$^{\text{arcsec}^{-1}}$)
(1)	(2)	(3)	(4)	(5)	(6)	(7)	(8)	(9)	(10)	(11)	(12)
LEGAC-86906([1])	10:02:13.375	02:12:41.19	0.82	0.75	20.01 (F814W)	0.92	5.8	11.84	295.5	1562.3	7.57
LEGAC-227516([1])	10:00:52.644	02:43:17.04	0.78	0.95	20.48 (F814W)	0.51	4.1	11.68	304.0	1534.7	7.44
S2F1-142([2])	03:06:36.511	−00:03:01.00	1.39	0.74	18.65 (F160W)	0.36	3.5	11.52	347.0	1737.9	8.43
UDS-29410([3])	02:17:51.220	−05:16:21.84	1.46	0.54	20.18 (F160W)	0.22	2.6	11.29	371.0	1743.0	8.45
CP-1243752([4])	10:00:17.746	02:17:52.71	2.09	0.79	20.82 (F160W)	0.34	4.5	11.66	350.0	1717.0	8.33

Column (1): Galaxy name with numerical superscripts indicate the primary reference for photometric parameters in Columns (1)–(8); ([1]) A. der Wel et al. (2021); ([2]) M. Longhetti et al. (2014); ([3]) J. de Sande et al. (2013); ([4]) M. Stockmann et al. (2020). Column (2): Right Ascension (J2000). Column (3): Declination (J2000). Column (4): Redshift estimated for each galaxy with photometric redshift for LEGA–C galaxies and spectroscopic redshift for others. Column (5): Observed axis ratio $q = b/a$. Column (6): Total apparent AB magnitude m in the specific observed band. Column (7): Effective (half-light) radius R_e in arcseconds. Column (8): Sérsic index n. Columns (9)–(10): Logarithm of the stellar mass (lg($M_\star/M_\odot$), and stellar velocity dispersion (σ_e) in km s^{-1}. Those values obtained from M. Cappellari (2023) for LEGAC-86906 and LEGAC-227516, from M. Longhetti et al. (2014) for S2F1-142, and from J. de Sande et al. (2013) for UDS 29 410 and CP-1243752. Column (11): Angular-diameter distance D_A in Mpc. Column (12): Physical scale in kpc arcsec^{-1} at the galaxy's redshift. Columns (11)–(12): D_A and physical scale are calculated from z_{spec} (Column 4) assuming a flat concordance ΛCDM cosmology ($H_0 = 70$ km s^{-1} Mpc^{-1}, $\Omega_m = 0.3$, $\Omega_\Lambda = 0.7$), using the calculator by E. L. Wright (2006).

expansion of the Universe causes the observed surface brightness of distant objects to decrease significantly, leading to lower signal-to-noise ratios (S/N) and increased measurement uncertainties. This sensitivity limit makes accurate dynamical measurements beyond the local Universe difficult with current facilities.

In this paper, we evaluate the potential of the ELT's cutting-edge capabilities to overcome these limitations. We begin by describing our galaxy sample selection and the intrinsic Sérsic models that form the basis of our study in Section 2. We then detail the simulation methodology for generating mock ELT observations with both MICADO and HARMONI in Section 3. The subsequent processing and analysis of these simulated data, including PSF determination from MICADO point source images, surface brightness parametrization of galaxy images, and stellar kinematic extraction from HARMONI data cubes, are presented in Section 4. Following this, Section 5 outlines the dynamical modelling techniques employed, using Jeans Anisotropic Models (JAM) and Markov chain Monte Carlo (MCMC) fitting, to recover SMBH masses from the processed data. Finally, in Section 6, we summarize our key findings, discuss the implications for future SMBH research at high redshifts, and assess the overall feasibility of these challenging but crucial measurements for understanding galaxy–BH co-evolution.

Although a factor of more than 10 improvement in angular resolution adopted in this study with the ELT HARMONI and MICADO nominally compensates for the ∼10 increase in angular diameter distance at $z \sim 1$–2, our results demonstrate that spatial resolution alone is insufficient to guarantee successful black hole mass measurements at high redshift. By modelling physically motivated galaxy populations appropriate for cosmic noon, and by explicitly accounting for surface-brightness dimming, adaptive-optics performance and PSF structure, wavelength-dependent instrumental effects, and realistic signal-to-noise limitations, we show that only a subset of massive, favourable systems can be dynamically probed. Our simulations therefore provide quantitative constraints on which galaxies are viable targets and under what observational conditions, establishing a realistic framework for future ELT studies that goes well beyond simple angular-resolution scaling from the local Universe.

We adopt a standard flat concordance ΛCDM Universe model in all calculations with $H_0 = 70$ km s^{-1} Mpc^{-1}, $\Omega_m = 0.3$, and $\Omega_\Lambda = 0.7$. To ensure consistency, we applied a foreground extinction correction using the method described by E. F. Schlafly & D. P. Finkbeiner (2011) and adopt the interstellar extinction law from J. A. Cardelli, G. C. Clayton & J. S. Mathis (1989) for all relevant quantities. Additionally, we used the AB photometric magnitude system (J. B. Oke 1974) throughout our analysis.

2 GALAXY SAMPLE AND SÉRSIC MODELS

2.1 High-redshift galaxy sample selection

To evaluate the capabilities of HARMONI and MICADO for measuring SMBH masses at high redshift, we selected a sample of galaxies within the range $1 \lesssim z \lesssim 2$. The primary selection criteria were the availability of essential observational data: spectroscopic redshift (z), high-resolution *HST* imaging, photometric parameters (total apparent magnitude, Sérsic profile parameters n and R_e), stellar mass ($M_\star$), and stellar velocity dispersion ($\sigma_\star$). Crucially, we targeted the brightest known quiescent, massive galaxies at these redshifts to maximize the S/N achievable in

realistic mock observations, mitigating the challenges posed by cosmological surface brightness dimming.

Candidate galaxies were sourced from several surveys. For $z \approx 1$, we utilized the Large Early Galaxy Astrophysics Census (LEGA–C) survey (A. der Wel et al. 2016, 2021). For $z \gtrsim 1.5$, we drew from various deep-field surveys targeting massive, quiescent galaxies, including the NEWFIRM Medium-Band Survey (NMBS; P. G. Dokkum et al. 2009; K. E. Whitaker et al. 2010), the UKIRT Infrared Deep Sky Survey (UKIDSS; A. Lawrence et al. 2007; R. J. Williams et al. 2009), KMOS and X-shooter spectroscopic campaigns (M. Stockmann et al. 2020), and VLT cluster surveys (J. de Sande et al. 2013; A. Beifiori et al. 2017), ensuring the availability of necessary *HST*/WFC3 imaging.

From these sources, we selected a representative sample of five galaxies, chosen as among the brightest known examples at their respective redshifts possessing the required data: two at $z \approx 1$ (LEGAC–86906, LEGAC–227516), two at $z \approx 1.5$ (S2F1–142, UDS 29410), and one at $z \approx 2$ (CP–1243752). Their detailed properties are listed in Table 1.

Even with next-generation facilities such as HARMONI and MICADO on the ELT, it will not be feasible to sample the $M_{\rm BH}$–σ relation across the full galaxy population in the same manner as in the local Universe. At high redshift, kinematically resolving the BH SOI will necessarily be restricted to the most massive, luminous, and structurally favourable systems, thereby probing only the 'tip of the iceberg' of the underlying population. Accordingly, the aim of this work is not to define a target sample size or to statistically map the evolution of the scaling relation, but rather to demonstrate that direct, spatially resolved measurements of $M_{\rm BH}$ will be achievable for a small yet critical subset of galaxies out to Cosmic Noon ($1 \lesssim z \lesssim 2$). Such measurements will provide essential anchor points for calibrating indirect $M_{\rm BH}$ estimators and for assessing potential evolution in the $M_{\rm BH}$–galaxy scaling relations. Determining how far these observational limits can be extended in terms of sample size and galaxy properties will ultimately depend on early ELT results and is beyond the scope of this study.

Fig. 2 shows the position of our selected sample (large coloured stars) on the mass–size diagram across three redshift bins, overlaid on the 3D-*HST* CANDELS sample (A. der Wel et al. 2014). This confirms our targets are massive and relatively compact, characteristic of quiescent galaxies at these epochs. Fig. 3 displays the archival *HST*/WFC3 F814W or F160W images for our sample. While large surveys contain numerous galaxies at these redshifts, most are fainter or lack the complete dataset needed for our detailed simulations, justifying our focus on these exceptionally bright systems.

2.2 Adopted intrinsic galaxy properties: Sérsic models

The light distribution of each galaxy is modelled using the Sérsic profile (J. L. Sersic 1968):

$$I(R) = I_{\rm e} \exp\left\{-b_n\left[\left(\frac{R}{R_{\rm e}}\right)^{1/n} - 1\right]\right\} \quad (1)$$

where n is the Sérsic index, $R_{\rm e}$ is the effective radius, and $I_{\rm e}$ is the intensity at $R_{\rm e}$. The term $b_n = Q^{-1}(2n, 1/2)$ is a coefficient, with Q^{-1} being the inverse regularized incomplete gamma function[2] (K. Zhu et al. 2025, equation 14), ensuring that $R_{\rm e}$ encloses half the total light. The parameters for each galaxy were previously published in the literature and are reproduced in Table 1. We assumed these Sérsic models represent the true intrinsic galaxy surface brightness as they were convolved with the *HST* PSF, down to the smallest radii resolvable with the ELT. These intrinsic models form the basis for the simulations of mock ELT observations detailed in the subsequent sections, where they are used as input for generating both MICADO images and HARMONI data cubes. This approach allows us to test the capabilities of ELT instrumentation in recovering galaxy and BH properties starting from well-defined, albeit idealized, galaxy profiles.

3 SIMULATING MOCK ELT OBSERVATIONS

3.1 Simulation strategy overview

The intrinsic galaxy properties, represented by the Sérsic models detailed in Section 2.2, form the foundation for our simulations of ELT observations. We use these models to generate realistic mock data for both the MICADO imager and the HARMONI integral-field spectrograph (IFS). This approach allows us to assess the ELT's capability to recover key galaxy parameters, including SMBH masses, from high-redshift galaxies. The following subsections describe the simulation process for each instrument.

3.2 Simulating MICADO imaging

MICADO (Multi-AO Imaging Camera for Deep Observations) is the ELT's first-light diffraction-limited imager, designed to deliver high sensitivity and a wide field of view (FoV, e.g. $\sim$ 50 arcsec $\times$ 50 arcsec with a fine pixel scale of a few milliarcseconds) across near-infrared (NIR) wavelengths (R. Davies et al. 2018; R. Davies et al. 2021). To simulate MICADO observations, we utilize the SIMCADO[3] software package (K. Leschinski et al. 2016). SIMCADO is a versatile tool that models the instrument's optical path, detector characteristics, and the effects of atmospheric turbulence corrected by AO.

The input to SIMCADO for our target galaxies are the 1D Sérsic surface brightness profiles described in Section 2.2, with the corresponding observed axial ratio. SIMCADO convolves these intrinsic light distributions with appropriate PSFs expected for MICADO, considering the chosen observing mode and the single-conjugate AO (SCAO[4]) using a natural guide star (NGS) performance.

In the SCAO mode, MICADO on the ELT is designed to deliver diffraction-limited NIR imaging (0.8–2.4 μm) by correcting atmospheric turbulence along the direction of a bright NGS. SCAO offers higher on-axis Strehl ratios than multi-conjugate AO (MCAO) over a smaller FoV, but performance depends on the guide star brightness and distance from the science target, with optimal results requiring a bright ($V \lesssim$ 15–16 mag) star within $\sim$15–20 arcsec of the field centre. Under nominal conditions, SCAO is expected to achieve on-axis Strehl ratios of $\gtrsim$60 per cent and FWHM of $\sim$10 mas in H band, with correspondingly sharp PSFs featuring a strong diffraction-limited core and extended wings due to residual wavefront errors. The PSF varies with field position and atmospheric conditions, and detailed PSF

[2]Implemented in scipy.special.gammainccinv

[3]https://pypi.org/project/SimCADO/

[4]https://simcado.readthedocs.io/en/latest/user_docs/9_PSFs.html

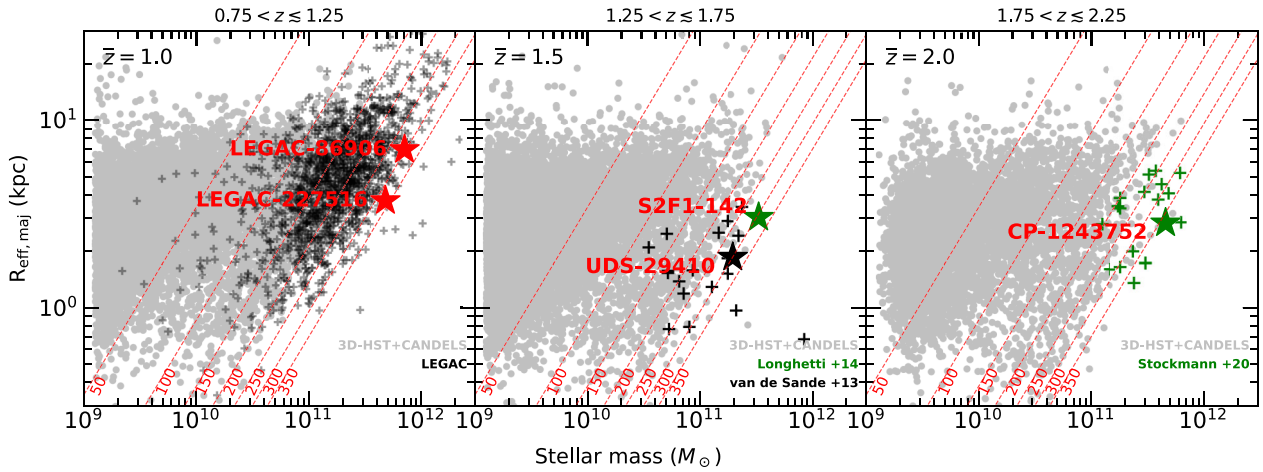

Figure 2. Our selected sample of five quiescent, massive, red-sequence galaxies (large coloured stars with red name tags; Table 1) is shown in the mass–size diagram, separated into three redshift panels: $z \approx 1$ (left), $z \approx 1.5$ (middle), and $z \approx 2$ (right). These galaxies are overlaid on the 3D-*HST* CANDELS sample (grey background points; A. der Wel et al. 2014), which is divided into corresponding redshift intervals ($0.75 < z \leq 1.25$, $1.25 < z \leq 1.75$, and $1.75 < z \leq 2.25$) and spans a stellar mass range of $2 \times 10^9 < M_\star < 2 \times 10^{12} M_\odot$. Red dashed inclined lines represent contours of constant stellar velocity dispersion from 50 to 350 km s^{-1}, estimated using the virial relation (M. Cappellari et al. 2006; D. Krajnović, M. Cappellari & R. M. McDermid 2018a; M. Cappellari 2023).

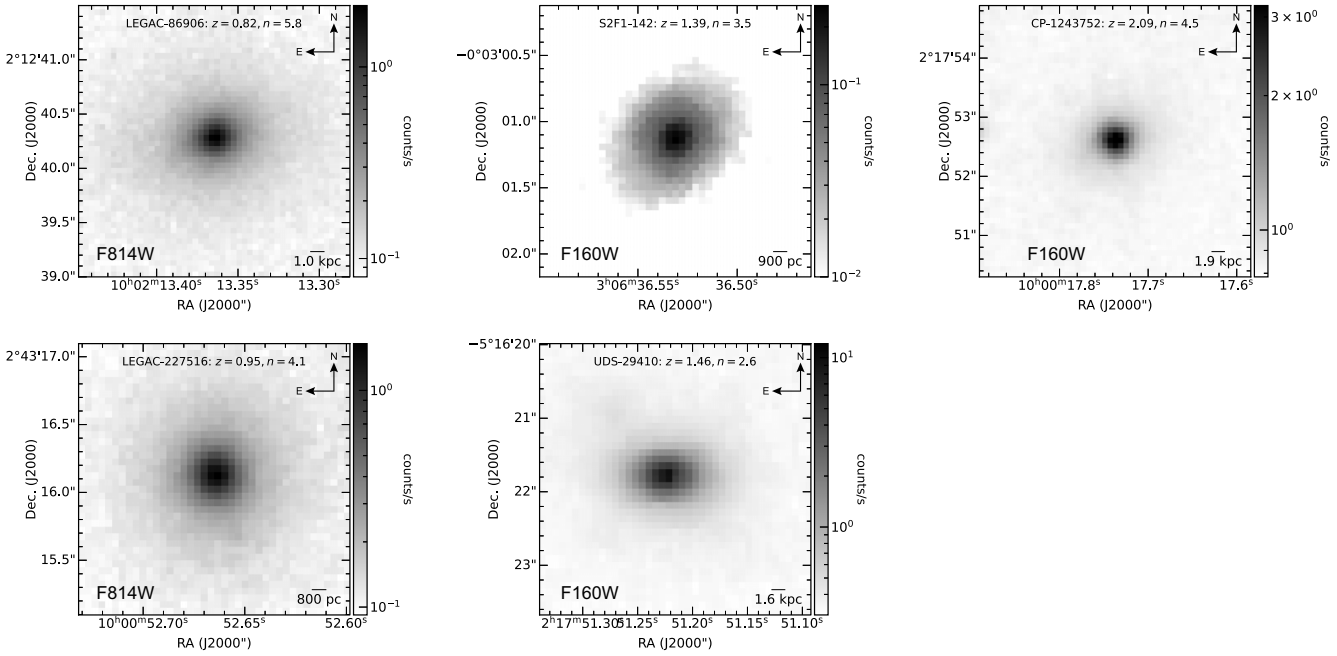

Figure 3. *HST*/WFC3 F814W and F160W images for five galaxies in our simulated sample are displayed in greyscale.

reconstruction algorithms aim to model these variations with ∼10–15 per cent precision in both Strehl and FWHM out to significant off-axis angles. This high-performance PSF is essential for accurately modelling the high-spatial-resolution surface brightness of galaxy nuclei, enabling the recovery of fine structural details and precise photometry required for robust SMBH mass measurements.

Realistic sky background levels and detector noise (read noise, dark current) are also incorporated to produce mock images that closely resemble actual MICADO observations. We produced images in either the *I* band or *H* band (Fig. 4), depending on redshift, which is close to the wavelength of the mock HARMONI data cubes. This is the same band we would need to observe in real data to ensure we capture the distribution of the tracer population, which is required by the dynamical models.

To generate the mock MICADO images, we first constructed emission curves based on the spectral energy distribution (SED) of an elliptical galaxy, adopting either the *I*- or *H*-band filter. The spectral axis was adjusted to account for the redshifts of the simulated galaxies by shifting the SEDs to longer wavelengths. Each galaxy was treated as a single source and modelled according to equation (1).

We then used the optical train implemented in SIMCADO to simulate the propagation of light from the galaxy through the

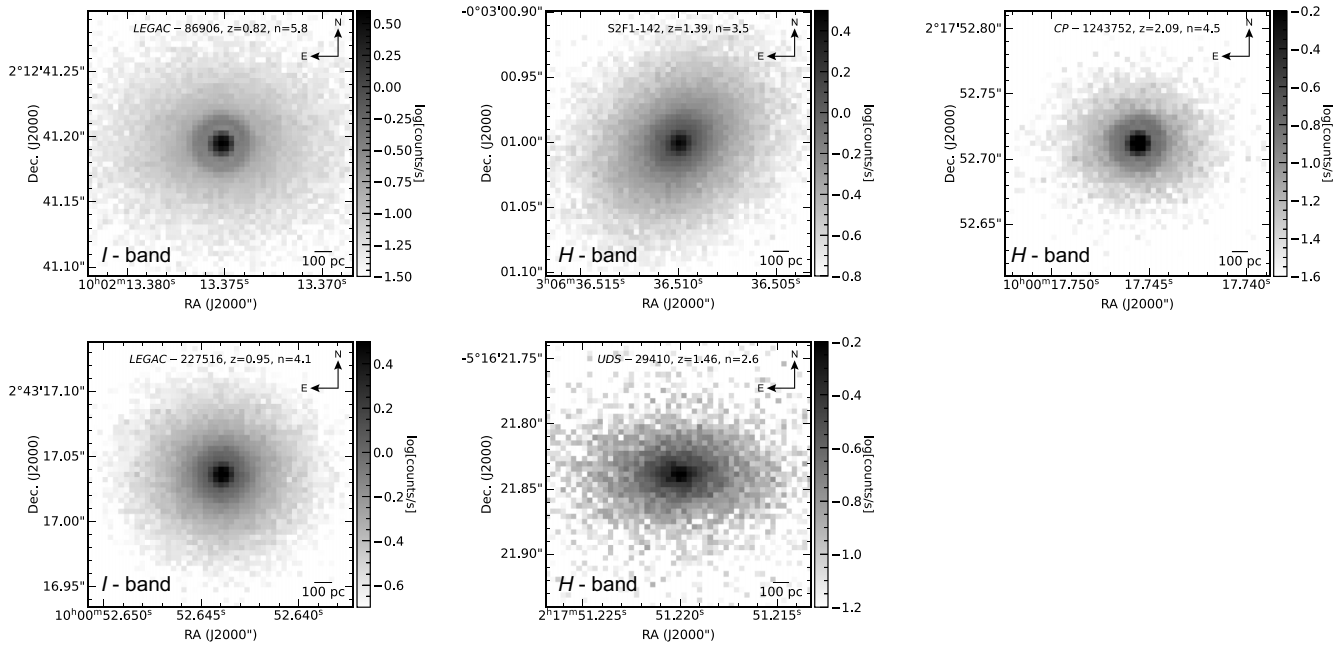

Figure 4. Greyscale mock MICADO images of the five simulated galaxies, produced using SIMCADO.

atmosphere, the ELT primary mirror, the instrument optics, and the detector. Detector and sky noise were added using the HxRG Noise Generator (HxRG NG), originally described by B. J. Rauscher (2015), which models the dominant noise components in NIR detectors, including white read noise, correlated and uncorrelated $1/f$ noise, alternating column noise, residual bias drifts, and so-called picture-frame noise. The resulting noise frames, expressed in electrons, were combined with the simulated signal to produce realistic mock images consistent with expected detector performance.

All simulations adopted a diffraction-limited point-spread function in SCAO mode, with a characteristic $\mathrm{FWHM_{PSF}} \simeq 10$ mas (R. Davies et al. 2021). To emulate realistic observing conditions, we fixed the exposure time per frame to `obs_dit` = 15 min and varied the number of exposures (`n_dit`). We find that `n_dit` = 4 provides optimal performance for all simulated galaxies, corresponding to a total on-source integration time of one hour, excluding target acquisition, overheads, and SCAO set-up.

The resulting mock MICADO images are then used to derive detailed Multi-Gaussian Expansion (MGE) surface brightness models of the stellar tracer population for the JAM dynamical models.

3.3 The HARMONI instrument and HSIM simulator

HARMONI is planned as the first-light IFS for the ELT, designed to operate across optical and NIR wavelengths (0.458–2.469 μm). It utilizes an image slicer integral field unit (IFU).

It is important to note that HARMONI is currently undergoing a rescoping review. This review process may result in modifications to the instrument's final specifications, which are not yet settled at the time of writing. The simulations presented in this paper are based on the latest well-defined specifications available prior to the conclusion of the rescoping review.

Based on these pre-review specifications, HARMONI was designed to offer four spatial scales (4×4, 10×10, 20×20, and 30×60 mas^2), corresponding to FoVs ranging from 0.86 arcsec × 0.61 arcsec to 9.12 arcsec × 6.42 arcsec. It was planned to provide three spectral resolving powers ($\lambda/\Delta\lambda \approx 3300$, 7100, and 17400) via 13 gratings (S. Zieleniewski et al. 2015). HARMONI will be coupled with AO systems – either SCAO using a NGS or laser tomography AO (LTAO)—to correct for atmospheric turbulence and achieve near-diffraction-limited performance (N. A. Thatte et al. 2016, 2020).

HARMONI aims to enable a wide range of science cases, including the study of galaxy kinematics and stellar populations at high redshift (S. Kendrew et al. 2016) and the measurement of black hole masses (D. D. Nguyen, M. Cappellari & M. Pereira-Santaella 2023; H. N. Ngo et al. 2025a, 2025b; D. D. Nguyen et al. 2025b), which are the focus of this work.

We generated mock HARMONI observations using the HSIM software[5] (S. Zieleniewski et al. 2015), a PYTHON pipeline designed specifically for HARMONI. HSIM takes high-resolution, noise-free input data cubes, which represent the intrinsic properties of astronomical sources, and simulates the effects introduced by the atmosphere, telescope, and instrument based on their specified characteristics. This simulation process includes applying wavelength-dependent PSFs, detector effects, and various noise sources to produce realistic output data resembling actual HARMONI observations.

3.4 Generating input noiseless data cubes

To generate the input noiseless data cubes for HSIM, we developed a dedicated PYTHON routine, `jam_mock_data_cube`[6]. This routine takes a calibrated MGE model (in $L_\odot \mathrm{arcsec}^{-2}$ for a given photometric band) and a stellar template spectrum

[5] v3.1 https://github.com/HARMONI-ELT/HSIM
[6] Available from https://github.com/micappe/jam_mock_data_cube

as primary inputs. It then produces a mock noiseless three-dimensional (3D) data cube, considering specified parameters for anisotropy, BH mass, and inclination.

In detail, we performed the following steps to create the noiseless data cubes:

(i) The initial one-dimensional (1D) Sérsic profile, with parameters from Table 1, is converted into an MGE using the `mge.fit_1d` procedure from the MGEFIT package[7] (M. Cappellari 2002). The input logarithmically sampled Sérsic profile is sampled from 0.01 to 100 times R_e and fitted with 15 Gaussians to ensure an accurate description of the galaxy's surface brightness profile Table 2.

(ii) This MGE model serves as input for the `jam.axi.proj` procedure within the JAM package[8] (M. Cappellari 2008, 2020). This step computes the two-dimensional (2D) kinematic fields (mean line-of-sight velocity V and velocity dispersion σ) for the given anisotropy, inclination, and BH mass. Specifically, JAM calculates the first (V) and second ($V_{\rm rms}$) velocity moments, from which the velocity dispersion is derived as $\sigma = \sqrt{V_{\rm rms}^2 - V^2}$.

(iii) The calculated kinematics are then used to construct a 3D data cube. This involves convolving the input stellar template spectrum with the line-of-sight velocity distribution (LOSVD) at each spatial position. The LOSVD is assumed to be a Gaussian function characterized by the mean velocity V and dispersion σ obtained in the previous step. This convolution is performed using the `varsmooth` function from the PPXF package[9] (M. Cappellari 2023), which accurately handles potential undersampling of the LOSVD. The resolution of the input templates is from three times smaller to comparable to the HARMONI resolution. In all cases, we request an output sampling in `jam_mock_data_cube` that is twice smaller than the HARMONI resolution, to ensure an accurate convolution with the line-spread function (LSF) within HSIM.

(iv) The routine then scales the flux of the input spectrum at each spatial pixel to match the observed surface brightness. This scaling utilizes the provided filter transmission curves along with the `ppxf_util.mag_sun` and `ppxf_util.mag_spectrum` functions from the PPXF package (M. Cappellari 2023) to ensure correct photometric calibration in the specified band.

(v) Finally, the routine assembles the fully convolved and scaled spectra into a 3D data cube with the desired spatial and spectral sampling, ready to be used as input for the HSIM simulator.

In our input to the `jam_mock_data_cube` routine, we adopted the following specifications:

(i) **SMBH mass estimation:** For each galaxy, the central $M_{\rm BH}$ for the HARMONI IFS simulation was estimated based on its $M_\star$ and σ_e. We used the relations from D. Krajnović et al. (2018b): equation (2) for $M_\star < M_{\rm crit}$ or equation (3) for $M_\star > M_{\rm crit} = 2 \times 10^{11}$ $M_\odot$.

(ii) **Dynamical anisotropy:** Consistent with observations that massive galaxies are generally characterized by low anisotropy (M. Cappellari 2026, fig. 10), we assumed an isotropic JAM model ($\beta_z = 0$) for generating the kinematics.

(iii) **Inclination:** Given the absence of published constraints on the inclinations of our five simulated targets, we adopted a uniform inclination of $i = 70^\circ$ for all systems in the JAM modelling when computing the 2D LOSVDs.

(iv) **Simulation FoV and spatial sampling:** Considering the cosmall apparent size of the target galaxies and our objective to resolve kinematics near the SMBH's SOI, the mock kinematic fields were generated for a central 0.4 arcsec $\times$ 0.4 arcsec FoV. To ensure accurate subsequent convolution with the instrumental PSF by HSIM, these models were computed on a fine grid with 2×2 mas^2 pixels, which is five times smaller than the 10×10 mas^2 HARMONI spaxel size used in the simulations.

(v) **PSF handling at input stage:** The LOSVDs generated by JAM were not convolved with any PSF at this stage, as PSF effects are incorporated later by the HSIM simulator.

(vi) **Stellar template selection:** The input stellar template spectrum for `jam_mock_data_cube` was taken from the C. Maraston & G. Strömbäck (2011) stellar population synthesis (SPS) models, based on the MARCS synthetic library (B. Gustafsson et al. 2008). For each galaxy, we selected a template with solar metallicity and an age that closely matched the known stellar population of the galaxy from Table 3.

3.5 Producing mock HARMONI IFS data cubes with HSIM

The previously generated input-noiseless cubes were then processed with HSIM to simulate mock HARMONI IFS observations using the $H + K$ grating. HSIM performs several key steps: it convolves the input cubes with the HARMONI PSF, and then rebins and interpolates the spectral and spatial dimensions to match the HARMONI spectral resolution for the $H + K$ grating and the adopted pixel scale of 10×10 mas^2.

These simulations assumed median observational conditions for the Armazones site, including the LTAO mode with a NGS of 17.5 mag in the H-band within a 30 arcsec radius. An optical zenith seeing at 0.5 μm with a FWHM of 0.64 arcsec and an airmass of 1.3 were assumed.

To emulate realistic observational strategies, multiple exposure frames and dithering patterns were applied. Each exposure utilized a Detector Integration Time (`DIT`) of 15 min. The total exposure time for each simulation was calibrated to achieve a minimum S/N of 5 per Å across the simulated FoV, and is determined by the number of exposures (`NDIT`) as Total Exposure Time = `DIT` × `NDIT`. All specific HSIM simulation parameters and conditions are detailed in Table 3.

4 ANALYSIS OF SIMULATED ELT DATA

Once the mock ELT observations (MICADO images and HARMONI data cubes) are generated as described in Section 3, the next crucial step is to process and analyse this simulated data, following the procedures we would apply to real data, to extract the physical parameters required for the dynamical modelling. This section outlines the methodologies used for deriving the PSF from simulated stellar images, parametrizing the galaxy surface brightness from simulated MICADO images, and extracting stellar kinematics from the simulated HARMONI data cubes.

4.1 PSF determination from simulated MICADO point source images

Accurate knowledge of the PSF is critical for deconvolving the observed galaxy light distribution and for reliable photometric

[7] v5.0: https://pypi.org/project/mgefit/
[8] v8.0: https://pypi.org/project/jampy/
[9] v9.4: https://pypi.org/project/ppxf/

Table 2. The Sérsic light-MGE models of five simulated galaxies.

j (1)	Galaxy (2)	$\lg \Sigma^{\rm lum}_{\star,j}$ ($L_\odot pc^{-2}$) (3)	$\lg \sigma_j$ (arcsec) (4)	$q'_j = b_j/a_i$ (5)	Galaxy (6)	$\lg \Sigma^{\rm lum}_{\star,j}$($L_\odot pc^{-2}$) (7)	$\lg \sigma_j$ (arcsec) (8)	$q'_j = b_j/a_i$ (9)
1	LEGAC-8906	4.463	−3.000	0.75	LEGAC-227516	4.053	−3.000	0.95
2		4.189	−2.630	0.75		3.874	−2.638	0.95
3		3.951	−2.318	0.75		3.712	−2.336	0.95
4		3.727	−2.029	0.75		3.559	−2.062	0.95
5		3.488	−1.751	0.75		3.392	−1.802	0.95
6		3.226	−1.482	0.75		3.199	−1.552	0.95
7		2.936	−1.220	0.75		2.977	−1.312	0.95
8		2.619	−0.966	0.75		2.724	−1.081	0.95
9	($z \approx 0.8213$)	2.274	−0.720	0.75	($z \approx 0.7794$)	2.438	−0.858	0.95
10	(I band)	1.899	−0.482	0.75	(I band)	2.118	−0.644	0.95
11		1.498	−0.252	0.75		1.763	−0.438	0.95
12		1.068	−0.028	0.75		1.373	−0.238	0.95
13		0.615	0.193	0.75		0.949	−0.039	0.95
14		0.135	0.431	0.75		0.477	0.178	0.95
15		−0.502	0.758	0.75		−0.209	0.475	0.95
1	S2F1-142	5.002	−3.000	0.74	UDS-29410	4.515	−3.000	0.54
2		4.861	−2.642	0.74		4.456	−2.650	0.54
3		4.730	−2.347	0.74		4.392	−2.364	0.54
4		4.608	−2.083	0.74		4.331	−2.113	0.54
5		4.473	−1.834	0.74		4.257	−1.879	0.54
6		4.312	−1.596	0.74		4.156	−1.658	0.54
7		4.120	−1.368	0.74		4.023	−1.447	0.54
8		3.896	−1.149	0.74		3.852	−1.247	0.54
9	($z \approx 1.386$)	3.636	−0.938	0.74	($z \approx 1.456$)	3.641	−1.056	0.54
10	(H band)	3.340	−0.737	0.74	(H band)	3.386	−0.873	0.54
11		3.005	−0.543	0.74		3.084	−0.700	0.54
12		2.632	−0.354	0.74		2.734	−0.532	0.54
13		2.221	−0.166	0.74		2.331	−0.363	0.54
14		1.745	0.041	0.74		1.828	−0.176	0.54
15		1.027	0.320	0.74		1.020	0.068	0.54
1	CP-1243752	6.101	−3.000	0.79				
2		5.861	−2.640	0.79				
3		5.643	−2.349	0.79				
4		5.448	−2.092	0.79				
5		5.252	−1.852	0.79				
6		5.039	−1.622	0.79				
7		4.802	−1.399	0.79				
8		4.538	−1.184	0.79				
9	($z \approx 2.090$)	4.247	−0.975	0.79				
10	(H band)	3.927	−0.773	0.79				
11		3.578	−0.577	0.79				
12		3.201	−0.385	0.79				
13		2.797	−0.192	0.79				
14		2.348	0.023	0.79				
15		1.691	0.325	0.79				

Column (1): Index j of the Gaussian component. Columns (2) and (6): Galaxy name (and redshift). Columns (3) and (7): Logarithm of the stellar surface luminosity density either in I or H bands, $\lg \Sigma^{\rm lum}_{\star,j}$ (in $L_\odot$ pc^{-2}). Columns (4) and (8): Logarithm of the Gaussian dispersion (width), $\lg \sigma_j$ (in arcseconds), along the major axis. Columns (5) and (9): Axial ratio, $q'_j = b_j/a_j$.

and structural analysis. For MICADO, the PSF will be complex and dependent on the AO system performance and observing conditions.

We simulate MICADO observations of point sources (stars) using SIMCADO under the same conditions anticipated for the galaxy observations. These simulated stellar images are then analysed to characterize the PSF. We use the MGE method, specifically the `mge.fit_sectors` routine from the MGEFIT PYTHON package (M. Cappellari 2002). The `mge.fit_sectors` algorithm models the 2D light distribution of the simulated star as a sum of co-axial Gaussian components. This MGE representation of the PSF is then used in the subsequent analysis of the simulated galaxy images to account for instrumental broadening.

4.2 MGE surface brightness parametrization from simulated MICADO galaxy images

The simulated MICADO images of the galaxies, generated as described in Section 3.2, provide high-resolution views of their stellar light distributions. To quantify their structure, we again employ the MGE method. The `mge.fit_sectors` routine is

Table 3. Mock HSIM IFS in the $H + K$ grating.

Galaxy name	*HST* image archival	Age (Gyr)	Metallicity [Fe/H]/MARCS	lgM_{BH}(2) ($M_\odot$)	lgM_{BH}(3) ($M_\odot$)	HSIM (NDIT)	HSIM$_{sensitivity}$ (NDIT)
(1)	(2)	(3)	(4)	(5)	(6)	(7)	(8)
LEGAC-86906([1])	(*I* band) F814W	4.5	0.0/z002	9.10	9.64	50	30
LEGAC-227516([1])	(*I* band) F814W	4.0	0.0/z002	9.18	9.54	80	50
S2F1-142([2])	(*H* band) F160W	2.3	0.0/z002	9.60	9.71	40	30
UDS 29410([3])	(*H* band) F160W	0.7	0.0/z002	9.48	9.93	40	30
CP-1243752([4])	(*H* band) F160W	2.6	0.0/z002	9.51	9.85	50	30

Column (1): Galaxy name. Column (2): Indicates if an archival *HST* image is available. Column (3): Assumed median stellar population age in Gyr. Ages for LEGA–C galaxies are from ([1]):M. Cappellari (2023); ages for other galaxies are from ([2]): M. Longhetti et al. (2014); ([3]): J. de Sande et al. (2013); ([4]): M. Stockmann et al. (2020). Column (4): Metallicity in terms of [Fe/H] and the corresponding MARCS synthetic stellar spectra library identifier. Given that the MARCS synthetic stellar spectra library does not include stellar populations younger than 3 Gyr, we adopt its 3 Gyr stellar template as the SPS model for the three galaxies at $z \gtrsim 1.5$ in the mock HSIM IFS simulations those have ages less than this age. Column (5): Estimated SMBH mass (in $M_\odot$) using equation (2) from D. Krajnović et al. (2018b) (applicable for $M_\star < M_{crit} \approx 2 \times 10^{11} M_\odot$). Column (6): Estimated SMBH mass (in $M_\odot$) using equation (3) from D. Krajnović et al. (2018b) (applicable for $M_\star > M_{crit}$). Column (7): Total number of exposures (NDIT) used in HSIM for the simulated HARMONI $H + K$ IFS observation. Each exposure has a duration of DIT = 15 min. Column (8): Sensitivity limit, expressed as the minimum number of exposures (NDIT), representing the lowest S/N from the simulated IFS for which PPXF can still extract accurate kinematics. All listed exposure times are science time on target and do not include overheads for target acquisition, LTAO set-up, or sky observations.

used to fit the 2D surface brightness distribution of each simulated galaxy.

Crucially, during this fitting process, the MGE model of the PSF (derived in Section 4.1) is convolved with the intrinsic MGE model of the galaxy before comparing with the simulated (PSF-convolved) MICADO galaxy image. This ensures that the derived MGE parameters represent the intrinsic galaxy structure, corrected for the effects of the PSF. The resulting MGE model (Fig. 5) is given in Table 4 and provides a compact and accurate description of the galaxy's surface brightness distribution, which serves as the stellar photometric component in the dynamical models used for SMBH mass determination (see Section 5).

4.3 Stellar kinematic extraction from simulated HARMONI data cubes

We derived the LOSVDs from the mock HARMONI IFS observations. For galaxies at redshifts $1 \lesssim z \lesssim 1.8$, the kinematics is mainly constrained by the Ca 2 Triplet (CaT) stellar absorption features, while for those at $z \gtrsim 1.8$, the strongest constraints come from the Mg 1b features. These prominent absorption lines fall within the spectral range of the $H + K$ grating used in our HSIM simulations, as illustrated in Fig. 6.

Prior to kinematic extraction, we applied adaptive Voronoi spatial binning to the simulated IFS data cubes using the VORBIN package[10] (M. Cappellari & Y. Copin 2003). This procedure groups spaxels to achieve a target S/N per bin per Å (detailed in Column 12 of Table 5), minimizing uncertainties in the subsequent LOSVD measurements.

Following spatial binning, each binned spectrum was logarithmically rebinned along the spectral dimension. We then employed the Penalized PiXel-Fitting (PPXF) software (M. Cappellari 2023) to fit these spectra using stellar population models by C. Maraston & G. Strömbäck (2011) based on the MARCS synthetic spectra (B. Gustafsson et al. 2008). To extract the mean velocity (V) and velocity dispersion (σ), we configured PPXF to fit only the first two velocity moments (V, σ) (moments = 2) while using additive polynomials (degree = 0), and no multiplicative ones (mdegree = -1). The instrumental broadening of the HARMONI IFS was accounted for by convolving the stellar templates with the differential instrumental dispersion. In the fit, we used 13 templates with ages spanning 3 to 15 Gyr (i.e. given that the youngest population of the MARCS synthetic spectra is 3 Gyr) and appropriate metallicities (see Table 3 for details). Fig. 6 displays the best-fitting SPS template overlaid on segments of the mock $H + K$ IFS spectra from the central bin of each of the five simulated galaxies, with residuals (data−model) shown as green dots. The resulting LOSVD maps (V, σ, and $V_{rms} = \sqrt{V^2 + \sigma^2}$) are presented in Figs 7, 8, and 9 for galaxy pairs at $z \approx 1$, 1.5, and 2, respectively.

For the targets at $z \approx 1$, we performed simulations with exposure times of 12.5 and 20 h for LEGAC-86906 and LEGAC-227516, respectively. For the galaxies at $z \approx 1.5$ (S2F1-142 and UDS 29410), the simulations were carried out with exposure times of 10 h, while for the galaxy at $z \approx 2$, an exposure time of 12.5 h was adopted (Table 3, excluding overheads). The mock IFS data attained sufficient S/N across the fitting spectral ranges. The choice of the brightest known targets at each redshift maximized sensitivity and optimized exposure times, making these durations representative for observations at these redshifts.

To validate our kinematic measurements, we compared the LOSVDs obtained using the CaT or Mg 1b features with those derived by fitting the entire $H + K$ spectral range, showing differences of less than 5 per cent. We further tested the kinematics using the empirical X-shooter Stellar Library Data Release 3 (XSL DR3; K. Verro et al. 2022), which includes stellar spectra from 683 stars covering 3000–25 000 Å at a resolution of $R \approx 10\,000$ (a factor of two coarser than MARCS). The XSL encompasses a wide variety of stellar types. The LOSVD maps derived using XSL templates showed differences of less than 8 per cent compared to those from the MARCS SPS models.

The signatures of central SMBHs are prominently seen in several central spaxels within the mock V_{rms} maps at the scales of the SMBH's SOI (at least several times larger than the proposed observational scale of 10 mas in this work) where its gravity dominates, characterized by the central peaks/drops towards the centre depending on whether its absence/presence or its large/small

[10] v3.2.1: https://pypi.org/project/vorbin/

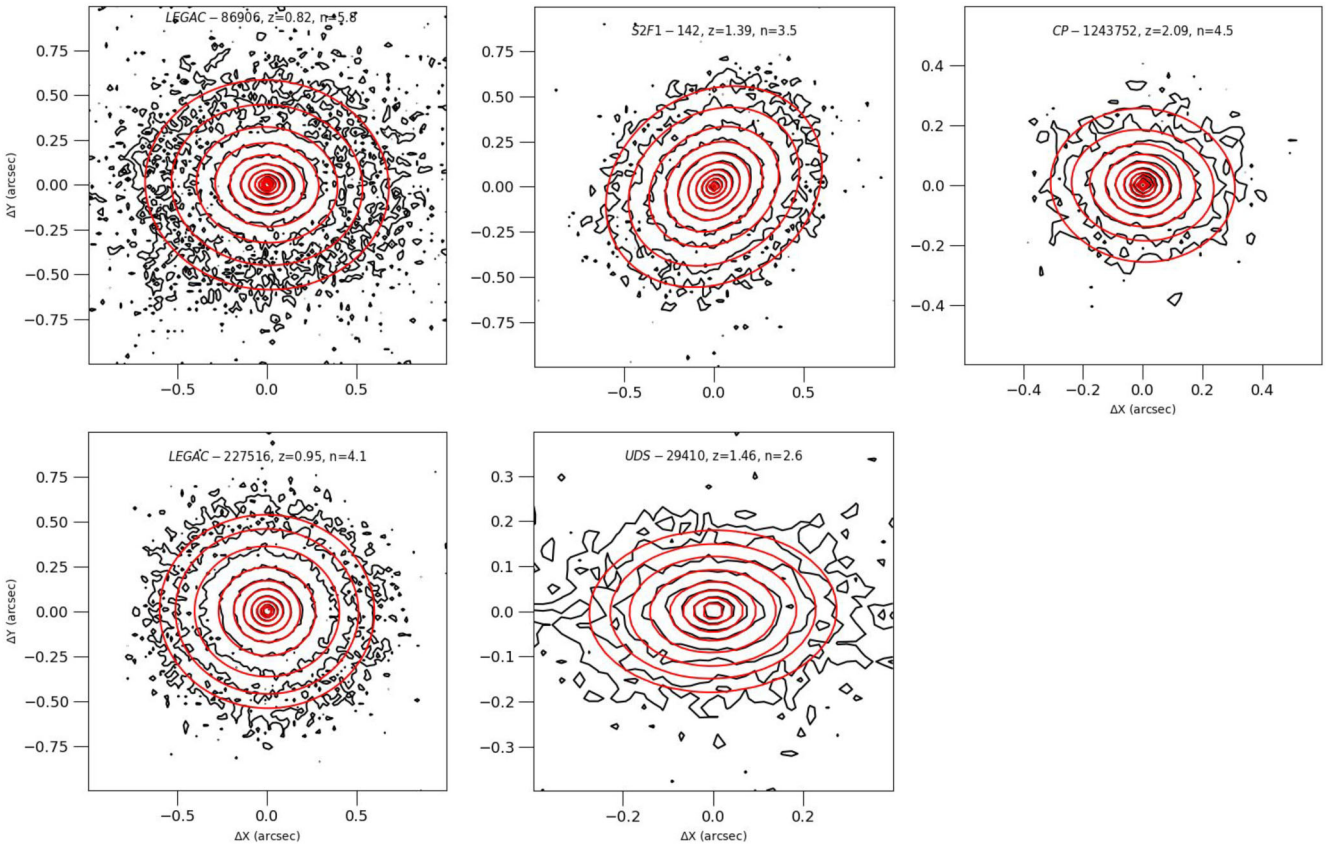

Figure 5. The comparison between the MICADO images produced by SIMCADO and their best-fitting MGE models for five simulated galaxies is presented in terms of 2D surface brightness density. Black contours represent the data, while red contours depict the model, illustrating the alignment between data and model at corresponding radii and contour levels which are spaced decreasing by 0.5 mag arcsec^{-1} outward.

Table 4. The mock MICADO mass-MGE models of five simulated galaxies.

j (1)	Galaxy (2)	$\lg \Sigma^{\rm mass}_{\star,j}(\mathrm{M}_\odot \mathrm{pc}^{-2})$ (3)	$\lg \sigma_j$ (arcsec) (4)	$q'_j = b_j/a_i$ (5)	Galaxy (6)	$\lg \Sigma^{\rm mass}_{\star,j}(\mathrm{M}_\odot \mathrm{pc}^{-2})$ (7)	$\lg \sigma_j$ (arcsec) (8)	$q'_j = b_j/a_i$ (9)
1	LEGAC-86906	5.748	−2.097	0.95	LEGAC-227516	5.570	−2.353	0.95
2		4.795	−1.656	0.95		5.019	−1.84	0.95
3		4.447	−1.391	0.95		4.719	−1.464	0.94
4	($z \approx 0.7794$)	4.189	−1.022	0.95	($z \approx 0.8213$)	4.451	−1.057	0.93
5	(I band)	3.827	−0.537	1.00	(I band)	3.998	−0.488	0.90
1	S2F1-142	5.311	−2.097	0.80	UDS-29410	5.041	−2.210	0.75
2		4.716	−1.641	0.80		4.844	−1.648	0.75
3		4.366	−1.371	0.80		4.496	−1.260	0.75
4	($z \approx 1.386$)	4.267	−1.127	0.80	($z \approx 1.456$)	4.206	−0.840	0.75
5	(H band)	3.961	−0.834	0.80	(H band)	–	–	–
6		3.569	−0.510	0.80		–	–	–
7		3.099	0.222	0.85		–	–	–
1	CP-1243752	5.819	−2.097	0.90	—	–	–	–
2		4.902	−1.620	0.90		–	–	–
3		4.569	−1.296	0.90		–	–	–
4		4.164	−0.952	0.90		–	–	–
5	($z \approx 2.090$)	3.552	−0.636	0.90		–	–	–
6	(H band)	3.231	−0.381	0.90		–	–	–
7		2.811	−0.222	0.95		–	–	–

Column (1): Index j of the Gaussian component. Columns (2) and (6): Galaxy name (and redshift). Columns (3) and (7): Logarithm of the stellar surface mass density, $\lg \Sigma^{\rm mass}_{\star,j}$ (in $\mathrm{M}_\odot$ pc^{-2}). Columns (4) and (8): Logarithm of the Gaussian dispersion (width), $\lg \sigma_j$ (in arcseconds), along the major axis. Columns (5) and (9): Axial ratio, $q'_j = b_j/a_j$.

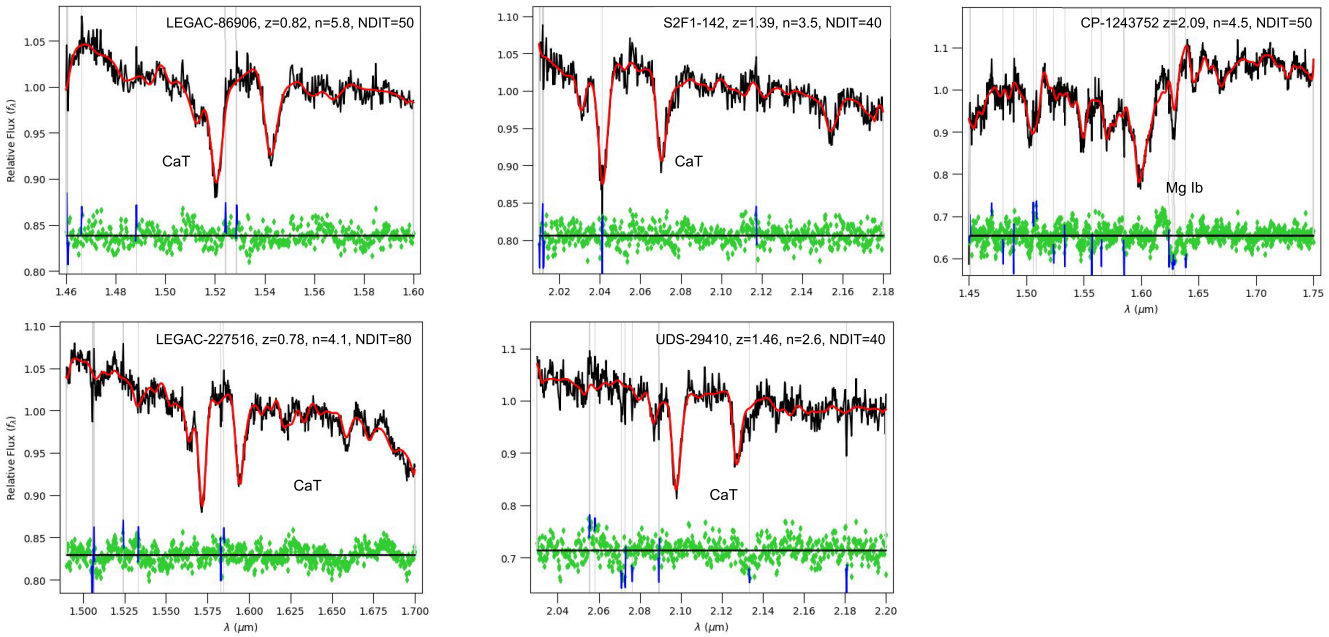

Figure 6. Examples of the $H + K$ HSIM mock spectra for five simulated galaxies are shown, including the targets at $z \approx 1$ (12.5-h exposure for LEGAC-86906 and 20-h exposure for LEGAC–27516), $z \approx 1.5$ (S2F1-142 and UDS-29410; 10-h exposures for both), and $z \approx 2$ (CP–1243752; 12.5-h exposure). The observed spectra (black) are fitted using PPXF (red), employing the stellar population models by C. Maraston & G. Strömbäck (2011) based on the MARCS synthetic spectra (B. Gustafsson et al. 2008). Prominent stellar absorption features, such as the CaT and Mg 1b lines, are marked in each panel. Fit residuals (i.e. `data–model`) are shown in green below each spectrum, highlighting the fit quality. Vertical grey lines indicate the locations of sky emission lines, which are masked during the fit. These regions produce significant residuals, shown in blue, due to the exclusion from the fitting process.

mass relative to the stellar mass distribution of the host galaxy. The contrast between the kinematics of these central spaxels and those at larger radii is visibly evident in all galaxies, irrespective of redshift. This highlights the exceptional spatial and spectral resolution and sensitivity capabilities of HARMONI in detecting the stellar kinematic signatures of SMBHs at redshifts of $1 \lesssim z \lesssim 2$, enabling their accurate dynamical mass measurements.

A detailed analysis of the σ maps reveals central drops in both stellar velocity dispersion σ and root-mean-squared velocity $V_{\rm rms}$ for targets at $z \lesssim 1$ (e.g. LEGAC-2346 and LEGAC-2408), consistent with those theorized in massive ellipticals by S. Tremaine et al. (1994), numerically predicted in local galaxies: with $z \leq 0.3$ (D. D. Nguyen et al. 2023), within $D \leq 10$ Mpc (D. D. Nguyen et al. 2025b), and within $10 < D \leq 20$ Mpc (H. N. Ngo et al. 2025a; H. N. Ngo et al. 2025b), or observationally proven in NGC 4736 with the *James Webb Space Telescope (JWST)* by D. D. Nguyen et al. (2025c). A key new finding is that for targets at $z \gtrsim 1.5$, no central σ drop is observed. Instead, $V_{\rm rms}$ either exhibits a central drop along the major axis due to significant rotational support (e.g. S2F1-142 and UDS 29 410 at $z \approx 1.5$) or continuously increases toward the centre for galaxies with intermediate rotation (e.g. CP-1243752 at $z \approx 2$) similar to what found in the local universe very recently with *JWST* (e.g. B. Tahmasebzadeh et al. 2025; M. A. Taylor et al. 2025; D. D. Nguyen et al. 2025a).

5 DYNAMICAL MODELLING AND SMBH MASS RECOVERY

This section details the process of measuring SMBH masses from the simulated HARMONI IFS and MICADO imaging data and assesses the instrument's sensitivity for such observations at high redshift. We first outline the methodology for recovering SMBH masses, then present the results and their validation, and finally discuss the HARMONI sensitivity limits.

5.1 Dynamical modelling with JAM

To determine the SMBH mass ($M_{\rm BH}$) and constrain other dynamical parameters, we compared the LOSVDs of the six simulated galaxies, derived in Section 4.3, with models generated by JAM (M. Cappellari 2008, 2020). Specifically, we focused on the maps of second velocity moments ($V_{\rm rms}$).

Our JAM models aimed to constrain four primary parameters: the $M_{\rm BH}$, the orbital anisotropy (β_z), a mass-scaling factor for the stellar component ($f_{\rm scale}$, expected to be close to 1), and the galaxy's inclination angle (i). To ensure efficient sampling of the parameter space, we adopted a logarithmic scale for $M_{\rm BH}$, while the other three parameters (β_z, $f_{\rm scale}$, i) were sampled on linear scales. The models accounted for the HARMONI LTAO PSF, characterized by a $\mathrm{FWHM_{PSF}} \approx 12$ mas. The search ranges for these parameters, along with their initial guesses for the JAM optimization, are detailed in Table 5.

We employed an MCMC approach, utilizing JAM, to explore the parameter space ($M_{\rm BH}$, β_z, $f_{\rm scale}$, i). This allowed us to identify the best-fitting values and determine their associated statistical and measurement uncertainties, as constrained by the mock HARMONI kinematics and the MICADO-derived stellar mass models. The MCMC simulations were performed within a Bayesian framework using the adaptive Metropolis algorithm (H. Haario, E. Saksman & J. Tamminen 2001), as implemented in the ADAMET[11] package (M. Cappellari et al. 2013). Each MCMC

[11] v2.0.9: https://pypi.org/project/adamet/

Table 5. Best-fitting JAM parameters and their associated uncertainties for six simulated galaxies.

Model	input $M_{\rm BH} = 0\,{\rm M}_\odot$			input $\log_{10} M_{\rm BH}(2)$			input $\log_{10} M_{\rm BH}(3)$			VORONOI	Number of
Parameters	Best fit	1σ	3σ	Best fit	1σ	3σ	Best fit	1σ	3σ	S/N	bins
(1)	(2)	(3)	(4)	(5)	(6)	(7)	(8)	(9)	(10)	(11)	(12)
					LEGAC-86906						
$\log_{10}(M_{\rm BH}/{\rm M}_\odot)$	3.92	±2.84	±4.22	9.00	±0.26	±0.45	9.64	±0.06	±0.15	76	32
$f_{\rm scale}$	1.02	±0.02	±0.06	1.00	±0.02	±0.05	1.01	±0.02	±0.06		
$i(^\circ)$	79.80	±9.80	±14.80	72.57	±10.10	±14.97	72.45	±11.51	±14.95		
β_z	0.06	±0.03	±0.10	0.06	±0.04	±0.09	0.07	±0.04	±0.10		
					LEGAC-27516						
$\log_{10}(M_{\rm BH}/{\rm M}_\odot)$	4.18	±2.97	±4.17	9.12	±0.13	±0.36	9.54	±0.06	±0.12	63	43
$f_{\rm scale}$	1.03	±0.01	±0.03	1.01	±0.01	±0.03	1.01	±0.01	±0.03		
$i(^\circ)$	57.58	±21.16	±29.87	67.37	±17.89	±29.70	57.35	±21.45	±29.75		
β_z	−0.01	±0.04	±0.16	−0.00	±0.02	±0.06	0.04	±0.04	±0.10		
					S2F1-142						
$\log_{10}(M_{\rm BH}/{\rm M}_\odot)$	3.91	±2.73	±4.18	9.50	±0.05	±0.14	9.71	±0.03	±0.08	55	64
$f_{\rm scale}$	1.00	±0.01	±0.03	1.01	±0.01	±0.04	1.01	±0.01	±0.04		
$i(^\circ)$	85.16	±4.86	±14.37	72.98	±10.91	±14.91	67.80	±12.12	±14.89		
β_z	0.03	±0.01	±0.06	0.07	±0.03	±0.08	0.07	±0.03	±0.07		
					UDS 29410						
$\log_{10}(M_{\rm BH}/{\rm M}_\odot)$	4.04	±2.75	±4.20	9.61	±0.07	±0.25	9.93	±0.06	±0.15	26	34
$f_{\rm scale}$	1.03	±0.01	±0.04	1.07	±0.02	±0.05	1.05	±0.02	±0.06		
$i\,(^\circ)$	86.78	±3.32	±6.68	79.69	±6.97	±12.08	73.09	±9.28	±13.97		
β_z	0.00	±0.02	±0.06	0.14	±0.06	±0.013	0.14	±0.11	±0.23		
					CP-1243752						
$\log_{10}(M_{\rm BH}/{\rm M}_\odot)$	4.18	±2.87	±4.41	9.51	±0.09	±0.28	9.86	±0.04	±0.11	46	26
$f_{\rm scale}$	1.01	±0.01	±0.03	1.09	±0.01	±0.05	1.01	±0.02	±0.05		
$i\,(^\circ)$	75.85	±9.67	±14.95	75.98	±10.07	±14.95	64.88	±9.39	±14.92		
β_z	0.10	±0.02	±0.06	0.07	±0.02	±0.07	0.09	±0.03	±0.09		

Note. We established consistent search ranges for the JAM parameters as follows: $\lg(M_{\rm BH}/{\rm M}_\odot)$: $0 \rightarrow 13$, $f_{\rm scale}$: $0.7 \rightarrow 1.3$, β_z: $-0.99 \rightarrow 1$, and i: $60^\circ \rightarrow 90^\circ$. Initial guesses: $M_{\rm BH} = 0{\rm M}_\odot$ and $\lg(M_{\rm BH}/{\rm M}_\odot) = 9.5$ for cases where the input mock kinematics without and with an SMBH, respectively, $f_{\rm scale} = 1.0$, $i(^\circ) = 70$, and $\beta_z = 0$. Column (1): Galaxy name. Columns (2)–(4) present the best-fitting parameters along with the 1σ (16–84 per cent) and 3σ (0.14–99.86 per cent) statistical and systematic uncertainties obtained from JAM when constrained using the HARMONI kinematics and MICADO stellar mass models. Here, the derived uncertainties are asymmetric as seen in Figs 10, 11, and 12; for consistency and transparency, we report symmetric errors corresponding to the larger asymmetric deviation in this table. These model constraints correspond to the case of no input black hole ($M_{\rm BH} = 0\,{\rm M}_\odot$). Columns (5)–(7) and (8)–(10) show the same information as Columns (2)–(4) but for cases where the input $M_{\rm BH}$ is computed using Eqs. (2) and (3) from D. Krajnović et al. (2018b), corresponding to $M_\star < M_{\rm crit} \approx 2 \times 10^{11}{\rm M}_\odot$ and $M_\star > M_{\rm crit}$, respectively. Columns (11)–(12) provide the target S/N per Å required for each bin (obtained in the spectral range around either the CaT ($z \lesssim 1.8$) or Mg 1b ($z > 1.8$) stellar absorption features) and the number of VORONOI kinematic bins that exceed the target S/N, respectively.

chain consisted of 3×10^4 iterations. The initial 20 per cent of these iterations were discarded as a burn-in phase, and the remaining 80 per cent were used to construct the posterior probability distribution function (PDF) for each parameter. The best-fitting parameters correspond to the highest likelihood region of this PDF. Uncertainties for all four parameters were calculated at the 1σ and 3σ confidence levels (CL), representing the 16–84 per cent and 0.14–99.86 per cent ranges of the PDF, respectively.

5.2 Results of SMBH mass recovery

The best-fitting JAM models and their associated statistical uncertainties are presented for two pairs and a single of simulated galaxies, grouped by redshift: $z \approx 1$ (LEGAC-86906 and LEGAC-227516; see Fig. 10), $z \approx 1.5$ (S2F1-142 and UDS 29410; see Fig. 11), and $z \approx 2$ (CP-1243752; see Fig. 12). These figures illustrate how well the best-fitting JAM models describe the stellar kinematics derived from the mock HSIM $H + K$ IFS gratings for different input $M_{\rm BH}$ values.

The figures feature 2D scatter plots for each pair of JAM parameters, where coloured points indicate their likelihood (white for maximum likelihood and 1σ CL, black for CLs larger than 3σ). Accompanying histograms show the 1D marginalized distributions for each parameter, from which the best-fitting values and their 1σ uncertainties (listed in Table 5) were derived. Inset plots located at the top-right corner of each main panel in these figures provide a direct comparison between the input $V_{\rm rms}$ map (from mock IFS data) and the $V_{\rm rms}$ map generated by the best-fitting JAM model. These comparisons use the same velocity scale for each galaxy and input $M_{\rm BH}$. The constrained models demonstrate good agreement with the mock kinematics across the simulated 0.4 arcsec × 0.4 arcsec HARMONI FoV, within the uncertainties of the mock kinematic measurements, irrespective of redshift. This finding is similar to previous studies by D. D. Nguyen et al. (2023) for targets at $z \leq 0.3$, D. D. Nguyen et al. (2025b) for targets within $D \leq 10$ Mpc, and H. N. Ngo et al. (2025a, 2025b) for galaxies in the distant range of $10 < D \leq 20$ Mpc. The characteristic kinematic signatures in the mock LOSVDs of these high-redshift targets, influenced by their SMBHs,

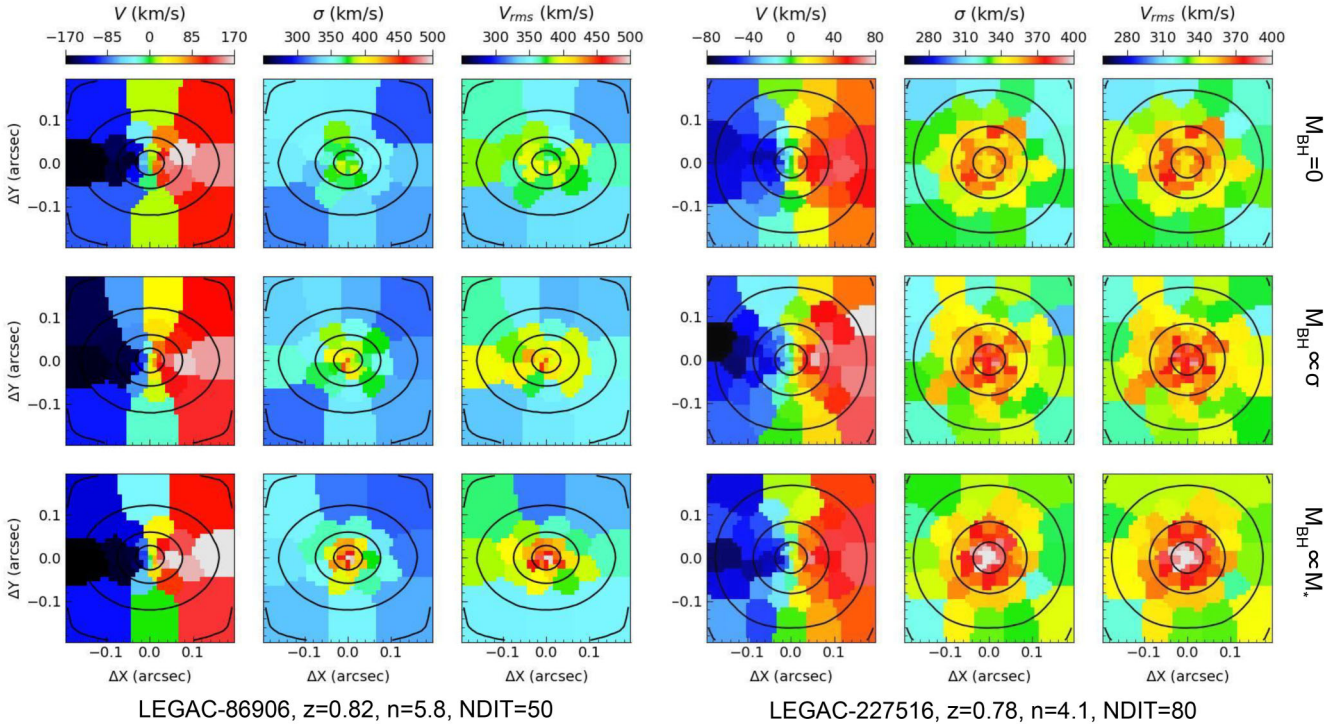

Figure 7. The kinematics of two simulated galaxies at redshift $z \approx 1$, LEGAC-86906 and LEGAC-227516, are extracted from the mock $H + K$ IFS data using the CaT stellar absorption features. The LOSVDs are presented from left to right as rotation (V), velocity dispersion (σ), and root-mean-square velocity ($V_{\rm rms}$). From top to bottom, they are shown for different $M_{\rm BH}$ cases: no black hole (top), $M_{\rm BH}$–σ predicted black hole (middle), and $M_{\rm BH}$–$M_\star$ predicted black hole (bottom). The black contours in all maps correspond to the isophotes derived from the collapsed HSIM IFS cubes, spaced in intervals of 1 mag arcsec^{-2}.

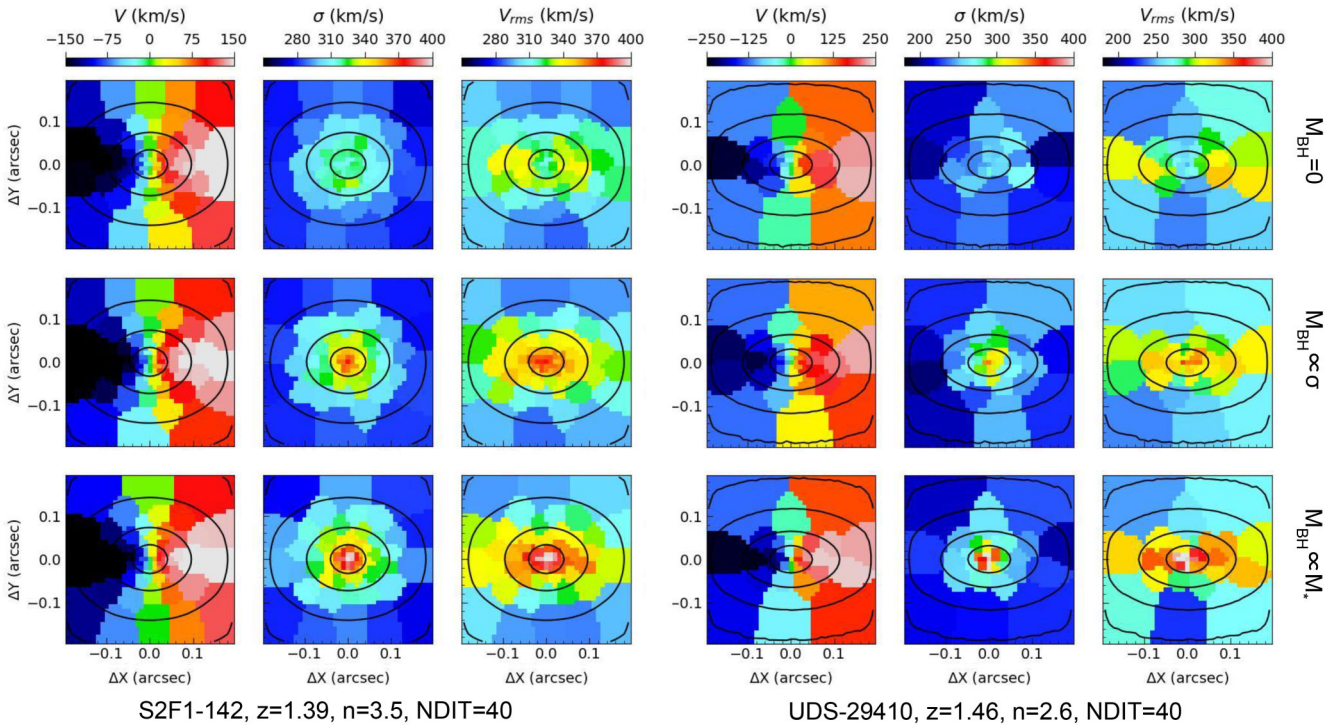

Figure 8. Same as Fig. 7 but displayed for two simulated galaxies at redshift $z \approx 1.5$: S2F1-142 and UDS 29410.

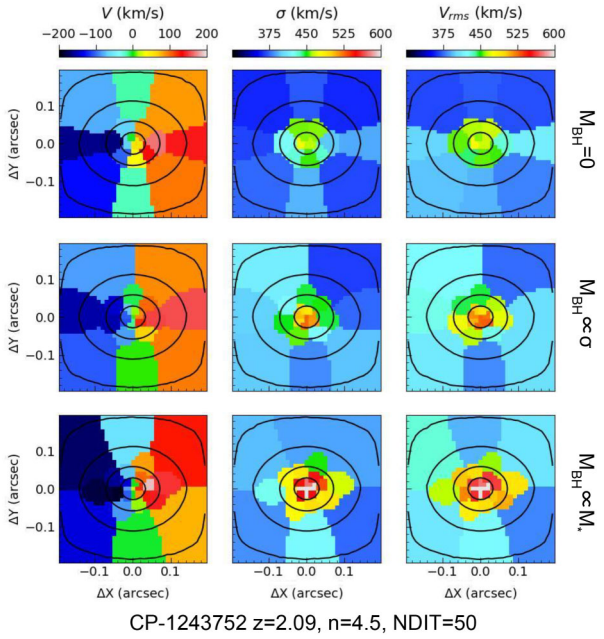

Figure 9. Same as Fig. 7 but displayed for the simulated galaxy at redshift $z \approx 2$: CP-1243752. Their LOSVDs are extracted from the mock $H + K$ IFS data using the Mg 1b stellar absorption features.

are successfully reproduced at the simulated 10 mas spaxel scale.

Notably, in the absence of a central SMBH ($M_{\rm BH} = 0$), the $V_{\rm rms}$ maps of galaxies at $z \lesssim 1$ (e.g. LEGAC-86906 and LEGAC-227516) exhibit central drops across at least 5–7 spaxels. As the input $M_{\rm BH}$ increases, these drops become shallower or transform into central peaks. Conversely, for the four galaxies at $z \gtrsim 1.5$ (S2F1-142, UDS 29410, and CP-1243752), even without a central SMBH, both the mock kinematics and the best-fitting JAM models show slightly increasing velocity dispersion (σ) maps towards the galaxy centre. In these cases, the presence of central drops or increases in the $V_{\rm rms}$ maps depends on the degree of rotational support.

The recovered $M_{\rm BH}$ does not converge to zero when the input $M_{\rm BH}$ is set to zero because the dynamical modelling is limited by uncertainties in the stellar kinematic measurements, as well as by other observational effects such as PSF convolution, throughput variations, AO performance, detector noise, and background noise. Measurement errors in the stellar LOSVDs (e.g. V and σ) – propagate through these effects and introduce a non-zero central mass component in the dynamical fit, even in the absence of a true SMBH. In practice, these uncertainties impose a noise floor on the minimum $M_{\rm BH}$ that can be reliably recovered. As a result, the modelling favours a small but nonzero $M_{\rm BH}$, which we interpret as an upper limit, to account for residual kinematic signatures within the central resolution element, thereby preventing convergence to exactly zero mass.

The recovered estimates for $M_{\rm BH}$ and $f_{\rm scale}$ closely match their input values used in the HSIM simulations, with differences typically below 10 per cent for both parameters. The quoted uncertainties are derived from the MCMC analysis of the $V_{\rm rms}$ maps and include statistical effects. The slightly lower accuracy compared to previous, similar works (e.g. D. D. Nguyen et al. 2023, 2025b; H. N. Ngo et al. 2025a, 2025b) can be attributed to the increased impact of background noise on observations of high-redshift sources, which leads to lower quality simulated kinematics. A well-known negative covariance between $M_{\rm BH}$ and $f_{\rm scale}$, often described as a 'banana shape' in the 2D PDF, is evident in the 3σ CL regions. This degeneracy arises from the interplay between the gravitational potential of the central SMBH and that of the host galaxy's stellar component: a larger BH mass can be compensated by a smaller stellar mass-scaling factor, and vice versa. The ability to characterize this degeneracy reflects the high spatial resolution of our simulations (10 mas observational scale), which is sufficient to resolve the SMBHs' SOIs up to $z \lesssim 2$. This success is also a testament to our selection of the brightest available targets from current surveys, ensuring adequate sensitivity and S/N to detect and measure the stellar kinematic signatures of SMBHs at these substantial distances. These results demonstrate that the ELT, with its advancements in spatial and spectral resolution, sensitivity, and AO capabilities, has the potential to extend dynamical SMBH measurements significantly beyond the local Universe, up to redshifts of $z \lesssim 2$.

The recovered values for the orbital anisotropy, β_z, are well constrained by the models, showing relatively small uncertainties. The results indicate a preference for slightly radial stellar orbits ($\beta_z \gtrsim 0$), with 3σ errors around ± 0.14. This is consistent with the isotropic value ($\beta_z = 0$) assumed as input in the mock data generation (see Section 3.4). The inclination angle (i) is less tightly constrained by the simulated data, though there is a tendency towards disky rotation (higher i values). These recovered inclinations are broadly consistent with the input values listed in Table 1.

It is not necessary to explore trade-offs in spectral (velocity) resolution in this work, as they are not expected to have a significant impact on the $M_{\rm BH}$ constraints for the systems considered here. In our modelling, all spectral pixels already contribute to the total χ^2 of the kinematic fits, such that additional spectral binning would primarily redistribute existing information rather than improve the effective S/N relevant for constraining the LOSVDs. Furthermore, for the massive galaxies targeted in this study, the intrinsic stellar velocity dispersions are large (Table 1, Column 10), and the adopted spectral resolution ($H + K$ grating with $R \sim 3300$) is already more than sufficient to resolve the relevant kinematic features. Consequently, the velocity resolution does not constitute a limiting factor in our analysis, and varying it within a reasonable range would not qualitatively alter our inferred $M_{\rm BH}$ or the conclusions drawn from these simulations.

5.3 Comparison of 1D kinematic profiles

To illustrate the agreement between our simulations and dynamical modelling, we compared the 1D radial profiles of $V_{\rm rms}$, as shown in Fig. 13. In this figure, data points represent the mean $V_{\rm rms}$ values extracted from the mock kinematic maps in concentric annuli (with 10 mas steps from the galaxy centre). The solid lines correspond to the $V_{\rm rms}$ values derived from the best-fitting JAM kinematic maps using the same annular extraction method. Kinematics for different input $M_{\rm BH}$ values are shown in distinct colours, applied consistently to both the mock data and the models. A key observation from these profiles is that the kinematic signatures of SMBHs are typically distinguishable within a radius of $\approx$50 mas.

Fig. 14 provides a consolidated comparison between the input $M_{\rm BH}$ values (see Table 3: column 5 for the predicted $M_{\rm BH}$ from the D. Krajnović et al. (2018a) $M_{\rm BH}$–σ relation and column 6 for the predicted $M_{\rm BH}$ from the D. Krajnović et al. (2018a) $M_{\rm BH}$–$M_\star$ relation) used in the HSIM simulations and the corresponding

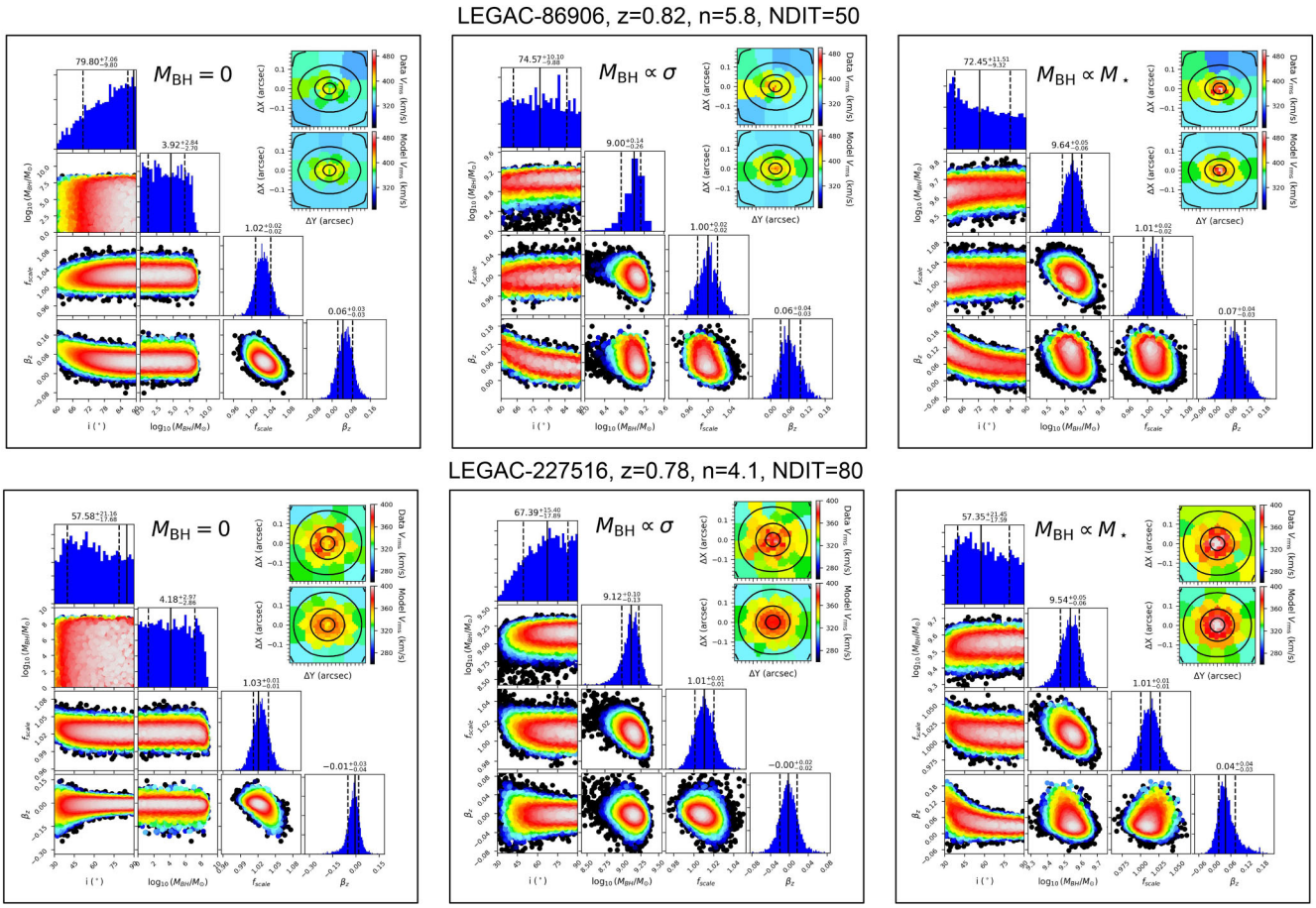

Figure 10. The PDFs obtained from the ADAMET MCMC optimization for the JAM models applied to the HSIM$H + K$ grating kinematics of two galaxies at $z \approx 1$, LEGAC-86906 (top row) and LEGAC-227516; (bottom row), illustrate the projected 2D distributions and 1D histograms of four free parameters: i, M_{BH}, f_{scale}, and β_z. Additionally, inset maps display the V_{rms} values. The top maps represent the kinematic maps extracted from the mock data cubes, while the bottom maps show the kinematic maps recovered from the best-fitting JAM model. The strong agreement across the HARMONI-simulated FoV confirms the robustness of the model constraints. The best-fitting JAM model is determined by the PDF with the highest likelihood, as presented in Table 5. Each row presents model constraints for different M_{BH} cases: no black hole (left), M_{BH}–σ predicted black hole (middle), and M_{BH}–$M_\star$ predicted black hole (right). The same LOSVD range is maintained in the colour bars for each galaxy to visualize the impact of central black hole mass on stellar kinematics. The black contours in the V_{rms} maps correspond to the isophotes derived from the collapsed HSIM IFS cubes, as similar as Fig. 7.

values recovered by the ADAMET MCMC algorithm coupled with JAM (see Table 5). The error bars represent the 3σ uncertainties, including both statistical and kinematic measurement uncertainties.

5.4 HARMONI sensitivity limit

We tested the sensitivity of HARMONI IFS for our selected galaxies at their respective redshifts by varying the on-source exposure time. Specifically, we repeated simulations, systematically reducing the `NDIT`, while fixed each `DIT = 15` min (thereby decreasing both the total exposure time, `NDIT` × `DIT`, and spectral S/N) until the resulting HARMONI IFS cubes produced reliable kinematic maps as shown in Figs. 7, 8, and 9 using PPXF. To enhance sensitivity when measuring the stellar kinematics using these newly testing cubes, we applied adaptive VORONOI binning, ensuring a targeted S/N $\approx$ 30/Å/measurement bin. This analysis allowed us to determine the required exposure times for each galaxy (Column 8 of Table 3). We note that, in these tests, the total apparent magnitudes of the five simulated galaxies were fixed to the observed values in the relevant photometric bands, as listed in Column 6 of Table 1, when constructing the input noiseless data cubes (see Section 3.4). When generating the mock observations with HSIM, the only parameter allowed to vary was `NDIT`.

The galaxy surface brightness profiles were derived from *HST* imaging (both parametric fits and direct measurements) and interpolated to match the proposed observational scales of 10 mas for HARMONI IFS and 4 mas for MICADO imaging using a Sérsic profile. Our analysis shows that the required on-source exposure time for reliable kinematic measurements scales with apparent brightness in the relevant filter. To establish the correspondence between on-source exposure time and total apparent magnitude, we artificially dimmed the total apparent magnitudes of our five simulated targets in either the I- or H-band images. Using the same procedure described in Section 3.4, we generated the corresponding input cubes for HSIM, thereby reducing the flux levels in the spectra of the noiseless data cubes. The resulting mock HSIM integral-field data exhibit lower spectral S/N, which in turn require larger values of `NDIT` (i.e. longer total on-source integration times) to recover the minimum spectral S/N necessary for reliable LOSVD measurements. We therefore varied `NDIT` in

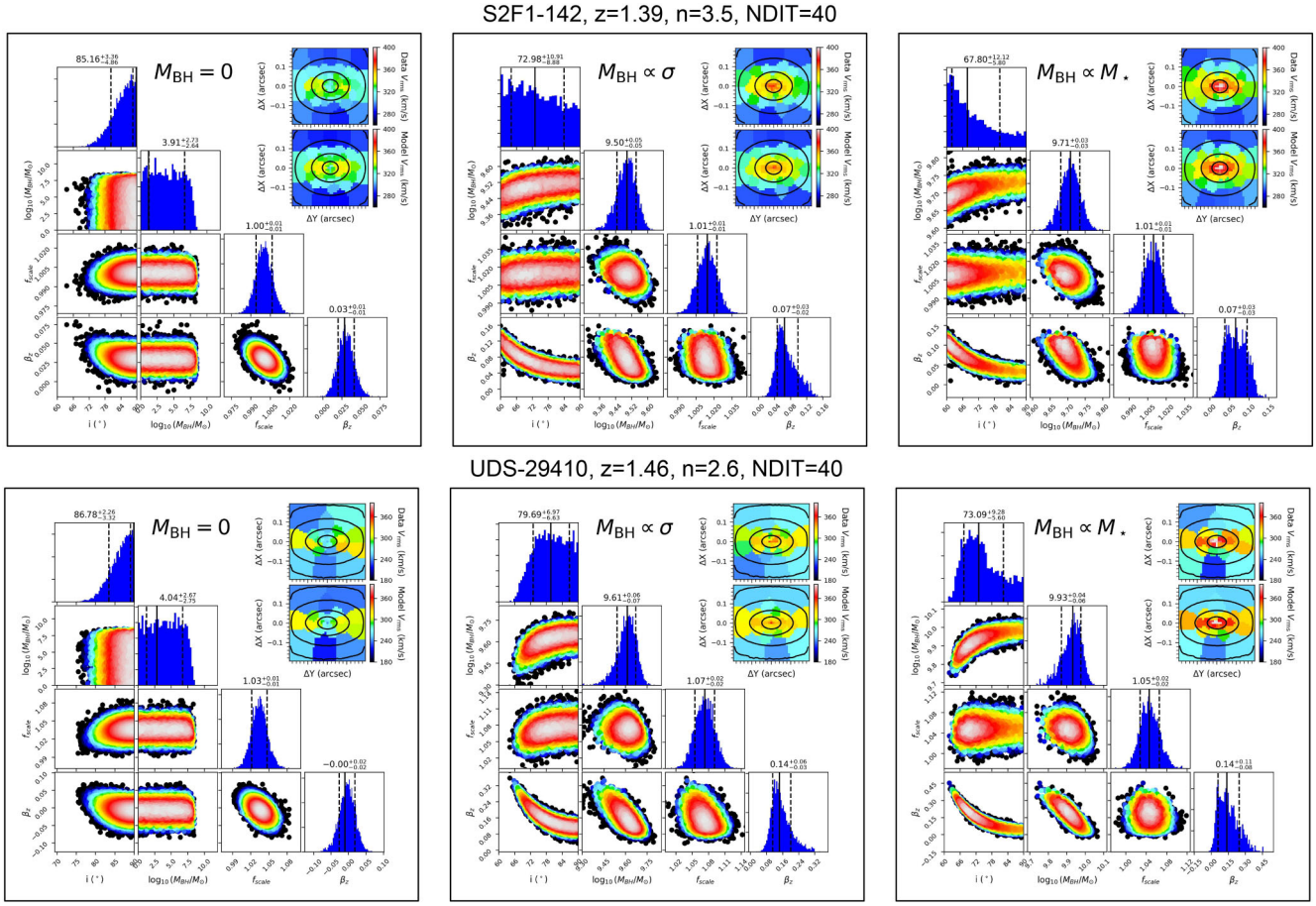

Figure 11. Same as Fig. 10 but for two simulated galaxies at redshift $z \approx 1.5$: S2F1-142 (top row) and UDS 29 410 (bottom row).

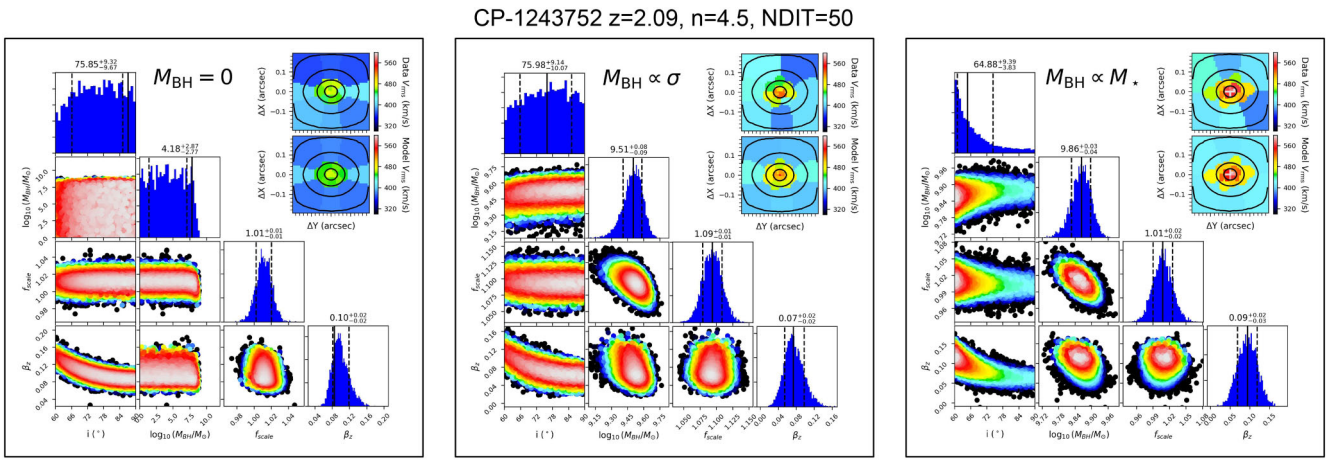

Figure 12. Same as Fig. 10 but for the simulated galaxy at redshift $z \approx 2$: CP-1243752.

HSIM until the simulated HARMONI data cubes yielded robust stellar kinematic maps when analysed with PPXF. From these tests, we find that for galaxies at $z \approx 1$ observed in the F814W band, total apparent magnitudes of 20 and 20.5 correspond to on-source integration times of approximately 5 and 7.5 h, respectively. In contrast, for galaxies observed in F160W at $1 < z \lesssim 2$, 5 h of on-source time is adequate to detect systems as faint as 20.8 mag. These results confirm the suitability of these targets for observations with the ELT. Given the careful simulation of MICADO imaging, our HARMONI IFS sensitivity estimates for the required exposure times are robust, supporting our SMBH survey at redshifts $z \approx 2$.

5.5 Importance of dynamically weighing SMBHs in distant universe

Spatially resolved dynamical measurements of black hole masses, using either stellar or cold gas kinematics, play a uniquely impor-

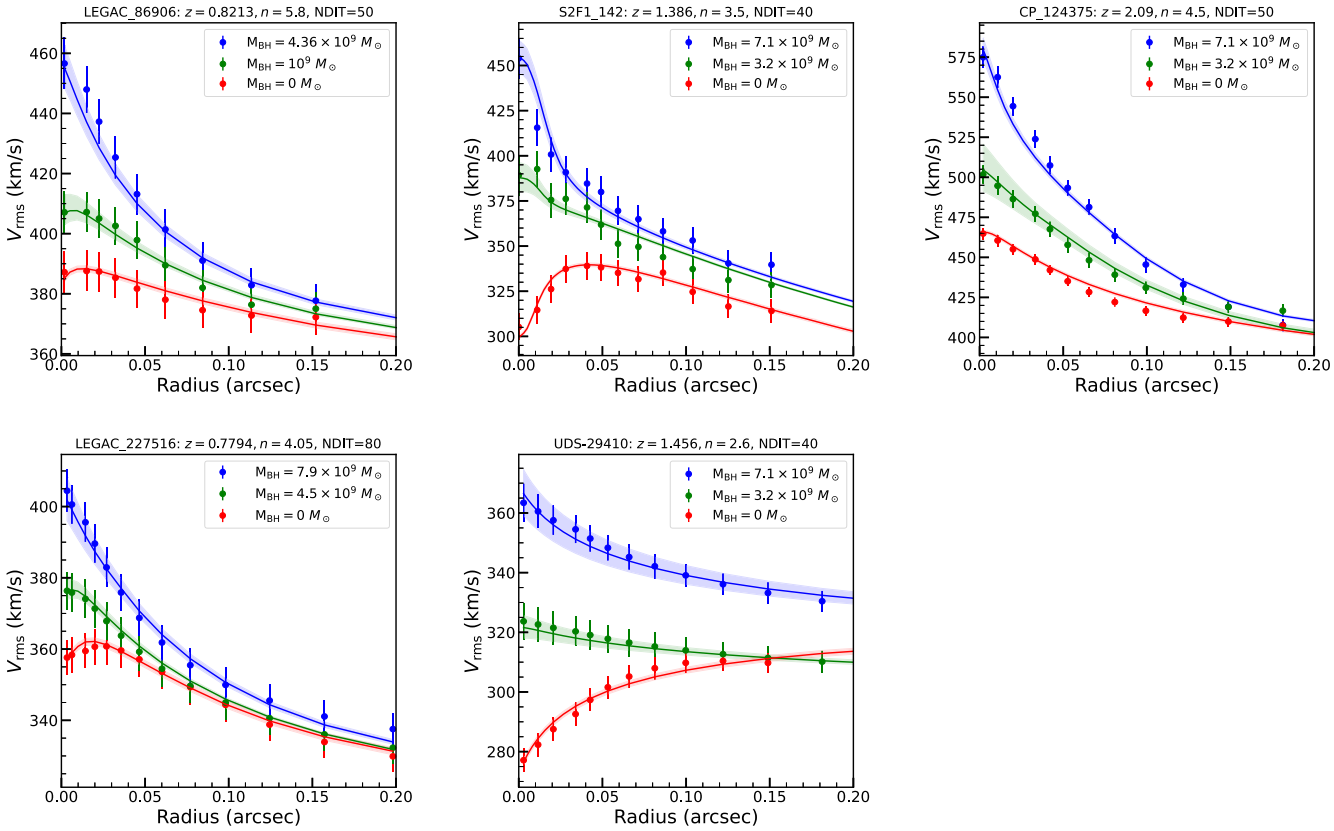

Figure 13. Comparisons of 1D kinematic profiles ($V_{\rm rms}$) extracted from the HSIM mock data cubes for all five selected galaxies. Profiles are shown for different input $M_{\rm BH}$: no BH (red), an $M_{\rm BH}$ –σ predicted BH (green), and an $M_{\rm BH}$–$M_\star$ predicted BH (blue). These are compared against their corresponding intrinsic kinematic profiles (same colour solid lines) derived directly from the best-fitting JAM models. The error bars and the shaded regions represent the 1σ uncertainties on the extracted kinematics of the HSIM mock data cubes and best-fitting JAM models, respectively. The profiles are extracted along the major axes of these galaxies.

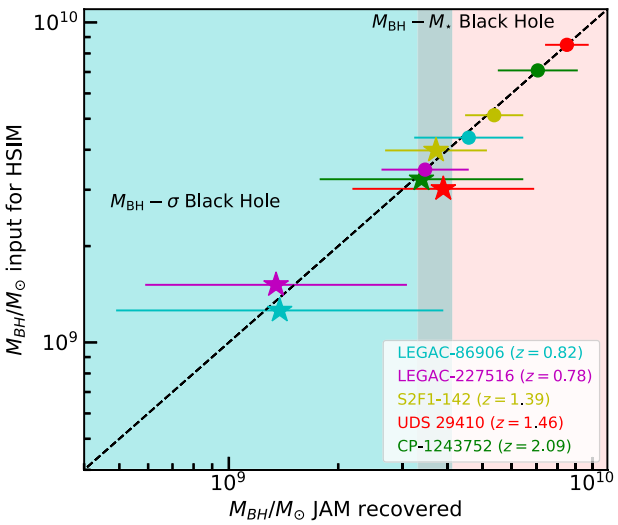

Figure 14. A summarized comparison of the input $M_{\rm BH}$ for HSIM and our recovered values at 3σ uncertainties. The black dashed line indicates the line of equality between the input $M_{\rm BH}$ for HSIM and our recoveries. Stars are $M_{\rm BH}$ that follows the $M_{\rm BH}$–σ relation, while dots are $M_{\rm BH}$ that follows the $M_{\rm BH}$–$M_\star$ relation (or equation 2 or 3 of D. Krajnović et al. 2018b, respectively).

tant role in anchoring our understanding of black hole growth across cosmic time. Unlike virial mass estimates for AGN and quasars, which depend on local empirical calibrations (e.g. reverberation mapping) and assumptions about geometry and dynamics, dynamical measurements rely directly on resolved gravitational motions and are therefore fundamentally calibration-independent. As such, they provide essential benchmarks for testing and refining indirect black hole mass estimators at high redshift. Establishing robust, kinematically measured black hole masses in increasingly distant galaxies – enabled by future facilities such as the 39m ELT and its advanced instruments, including the HARMONI spectrograph and the MICADO imager – is therefore critical for shaping black hole physics studies in the next decades by (i) assessing the true evolution of galaxy – black hole scaling relations and (ii) disentangling physical growth from observational bias in studies of black hole–galaxy co-evolution.

6 CONCLUSIONS

This paper investigated the feasibility of extending direct SMBH mass measurements to high-redshift ($1 \lesssim z \lesssim 2$) galaxies using the capabilities of the upcoming ELT with its first-light instruments, MICADO and HARMONI. We developed a comprehensive simulation pipeline, generating mock MICADO images and HARMONI IFS data for a sample of five bright, massive, quiescent galaxies. These simulations incorporated realistic instru-

mental effects, observational conditions, and JAM for stellar dynamics.

Our principal findings are:

(i) **High-fidelity mass models with MICADO:** Simulated MICADO observations, with an angular resolution of ≈ 10 mas ($\mathrm{FWHM_{PSF}}$) and a 4 mas pixel scale, demonstrate that detailed stellar mass models, essential for dynamical studies, can be derived from approximately one hour of on-source exposure time per galaxy in the I or H band. The resulting surface brightness profiles are consistent with existing *HST* data and provide the necessary resolution to probe the central regions of high-redshift galaxies.

(ii) **Resolving kinematics with HARMONI:** Mock HARMONI IFS observations, simulated using the $H+K$ grating at a 10 mas spaxel scale, successfully yielded stellar kinematic maps ($V, \sigma, V_{\rm rms}$) of sufficient quality. These kinematics, primarily extracted from CaT features (for $z \lesssim 1.8$) or Mg 1b features (for $z \approx 2$), clearly revealed the gravitational influence of central SMBHs. We observed distinct kinematic signatures, such as central drops or peaks in $V_{\rm rms}$ maps, depending on the SMBH mass and host galaxy properties, even at these substantial distances.

(iii) **Accurate SMBH mass recovery:** By applying JAM-based dynamical models within an MCMC framework to the simulated HARMONI $V_{\rm rms}$ maps, we demonstrated that SMBH masses can be recovered with good accuracy. For our sample of bright, massive galaxies, the recovered $M_{\rm BH}$ values typically agreed with the input simulation values to within $\sim$10 per cent up to $z \approx 2$. The models also constrained other dynamical parameters, such as the stellar mass-scaling factor and orbital anisotropy, highlighting the robustness of the method.

(iv) **Observational requirements and sensitivity:** We quantified the sensitivity of HARMONI, determining the minimum on-source exposure times required to obtain reliable stellar kinematics for SMBH mass measurements. These exposure times scale with the apparent brightness in the observed filter. For galaxies at $z \approx 1$ observed in F814W, total magnitudes of 20–20.5 correspond to integration times of approximately 5–7.5 h, while for F160W at $1 < z \lesssim 2$, 5 h is sufficient to reach galaxies as faint as 20.8 mag. These limits establish practical exposure thresholds for future kinematic studies of distant galaxies and ensure sufficient S/N in the extracted spectra to mitigate the effects of cosmological surface brightness dimming and sky background.

(v) **A Framework for future ELT studies:** The simulation tools and methodologies presented, including the `jam_mock_data_cube` routine, provide a robust framework for planning and interpreting future ELT observations. This work supports the potential of the ELT to significantly advance our understanding of SMBH demographics and their co-evolution with galaxies by extending direct dynamical measurements well beyond the local Universe.

In summary, our simulations affirm that the ELT, with MICADO and HARMONI, possesses the transformative capability to directly measure SMBH masses in massive quiescent galaxies at $1 \lesssim z \lesssim 2$. These pioneering observations will be crucial for empirically testing the evolution of SMBH-galaxy scaling relations and providing new insights into the processes that govern galaxy formation and evolution across cosmic time.

DATA AVAIBILITY

All data and software used in this paper are public. We provided their links in the text when discussed.

ACKNOWLEDGEMENTS

The authors would like to thank the anonymous referee for their careful reading and useful comments, that helped to improve the paper greatly. We are grateful to Prof. van de Sande for providing the 3D-HST+CANDELS data used in Fig. 2. NT would like to acknowledge partial support from UKRI grant ST/X002322/1 for UK ELT Instrument Development at Oxford. MPS acknowledges support under grants RYC2021-033094-I, CNS2023-145506, and PID2023-146667NB-I00 funded by MCIN/AEI/10.13039/501100011033 and the European Union Next Generation EU/PRTR.

Facilities: HST/WFC3.

Software: PYTHON 3.12 (G. Van Rossum & F. L. Drake 2009), MATPLOTLIB 3.6 (J. D. Hunter 2007), NUMPY 1.22 (C. R. Harris et al. 2020), SCIPY 1.3 (P. Virtanen et al. 2020), PHOTUTILS 0.7 (L. Bradley et al. 2024), ASTROPY 5. 1(Astropy Collaboration 2022), ADAMET 2.0 (M. Cappellari et al. 2013), JAMPY 7.2 (M. Cappellari 2020), PPFX 8.2 (M. Cappellari 2023), VORBIN 3.1 (M. Cappellari & Y. Copin 2003), MGEFIT 5.0 (M. Cappellari 2002), HSIM 3.11 (S. Zieleniewski et al. 2015), and SIMCADO (K. Leschinski et al. 2016).

REFERENCES

Ahn C. P. et al., 2018, ApJ, 858, 102
Astropy Collaboration et al., 2022, ApJ, 935, 167
Barth A. J., Sarzi M., Rix H.-W., Ho L. C., Filippenko A. V., Sargent W. L. W., 2001, ApJ, 555, 685
Barth A. J., Boizelle B. D., Darling J., Baker A. J., Buote D. A., Ho L. C., Walsh J. L., 2016, ApJ, 822, L28
Beifiori A. et al., 2017, ApJ, 846, 120
Bradley L. et al., 2024, astropy/photutils: 2.0.2
Cappellari M., 2002, MNRAS, 333, 400
Cappellari M., 2008, MNRAS, 390, 71
Cappellari M., 2020, MNRAS, 494, 4819
Cappellari M., 2023, MNRAS, 526, 3273
Cappellari M., 2026, in Encyclopedia of Astrophysics. Elsevier, Amsterdam, p. 122
Cappellari M., Copin Y., 2003, MNRAS, 342, 345
Cappellari M. et al., 2006, MNRAS, 366, 1126
Cappellari M., Neumayer N., Reunanen J., van der Werf P. P., de Zeeuw P. T., Rix H.-W., 2009, MNRAS, 394, 660
Cappellari M. et al., 2013, MNRAS, 432, 1709
Cardelli J. A., Clayton G. C., Mathis J. S., 1989, ApJ, 345, 245
Davies R. et al., 2010, in McLean I. S., Ramsay S. K., Takami H., eds, Proc. SPIE Conf. Ser. Vol. 7735, Ground-based and Airborne Instrumentation for Astronomy III. SPIE, Bellingham, p. 77352A
Davies R. et al., 2018, in Evans C. J., Simard L., Takami H., eds, Proc. SPIE Conf. Ser. Vol. 10702, Ground-based and Airborne Instrumentation for Astronomy VII. SPIE, Bellingham, p. 107021S
Davies R. et al., 2021, The Messenger, 182, 17
Davis T. A. et al., 2020, MNRAS, 496, 4061
de Zeeuw T., 2001, in Kaper L., Heuvel E. P. J. V. D., Woudt P. A., eds, Black Holes in Binaries and Galactic Nuclei. Springer-Verlag, Berlin, p. 78
Fabian A. C., 2012, ARA&A, 50, 455
Ferrarese L., Merritt D., 2000, ApJ, 539, L9
Gebhardt K. et al., 2000, ApJ, 539, L13
Gebhardt K. et al., 2003, ApJ, 583, 92

Greene J. E., Strader J., Ho L. C., 2020, ARA&A, 58, 257
Gustafsson B., Edvardsson B., Eriksson K., Jørgensen U. G., Nordlund Å., Plez B., 2008, A&A, 486, 951
Haario H., Saksman E., Tamminen J., 2001, Bernoulli, 7, 223
Harris C. R. et al., 2020, Nature, 585, 357
Hunter J. D., 2007, Comput. Sci. Eng., 9, 90
Imanishi M. et al., 2020, ApJ, 902, 99
Izumi T. et al., 2020, ApJ, 898, 75
Kendrew S. et al., 2016, MNRAS, 458, 2405
Kormendy J., Ho L. C., 2013, ARA&A, 51, 511
Kormendy J., Richstone D., 1995, ARA&A, 33, 581
Krajnović D., Cappellari M., McDermid R. M., 2018a, MNRAS, 473, 5237
Krajnović D. et al., 2018b, MNRAS, 477, 3030
Lawrence A. et al., 2007, MNRAS, 379, 1599
Leschinski K. et al., 2016, in Angeli G. Z., Dierickx P., eds, Proc. SPIE Conf. Ser. Vol. 9911, Modeling, Systems Engineering, and Project Management for Astronomy VI. SPIE, Bellingham, p. 991124
Longhetti M., Saracco P., Gargiulo A., Tamburri S., Lonoce I., 2014, MNRAS, 439, 3962
Magorrian J. et al., 1998, AJ, 115, 2285
Maiolino R. et al., 2024, A&A, 691, A145
Maraston C., Strömbäck G., 2011, MNRAS, 418, 2785
McConnell N. J., Ma C.-P., Gebhardt K., Wright S. A., Murphy J. D., Lauer T. R., Graham J. R., Richstone D. O., 2011, Nature, 480, 215
Ngo H. N., Nguyen D. D., Nguyen T. N., Dang T. H., Ho T. H. T., 2025a, preprint (arXiv:2509.03364)
Ngo H. N., Nguyen D. D., Le T. T. Q., Ho T. H. T., Nguyen T. N., Dang T. H., 2025b, Universe, 11 360
Ngo H. N. et al., 2025c, ApJ, 992, 211
Nguyen D. D., 2017, preprint (arXiv:1712.02470)
Nguyen D. D., 2019, in ALMA2019: Science Results and Cross-Facility Synergies, p. 106
Nguyen D. D., Seth A. C., Reines A. E., den Brok M., Sand D., McLeod B., 2014, ApJ, 794, 34
Nguyen D. D. et al., 2017, ApJ, 836, 237
Nguyen D. D. et al., 2018, ApJ, 858, 118
Nguyen D. D. et al., 2019, ApJ, 872, 104
Nguyen D. D. et al., 2020, ApJ, 892, 68
Nguyen D. D. et al., 2021, MNRAS, 504, 4123
Nguyen D. D. et al., 2022, MNRAS, 509, 2920
Nguyen D. D., Cappellari M., Pereira-Santaella M., 2023, MNRAS, 526, 3548
Nguyen D. D. et al., 2025a, preprint (arXiv:2509.20519)
Nguyen D. D. et al., 2025b, AJ, 170, 124
Nguyen D. D. et al., 2025c, A&A, 698, L9
Oke J. B., 1974, ApJS, 27, 21
Onishi K., Iguchi S., Davis T. A., Bureau M., Cappellari M., Sarzi M., Blitz L., 2017, MNRAS, 468, 4663
Rauscher B. J., 2015, PASP, 127, 1144
Rusli S. P. et al., 2013, AJ, 146, 45
Saglia R. P. et al., 2016, ApJ, 818, 47
Schlafly E. F., Finkbeiner D. P., 2011, ApJ, 737, 103
Sersic J. L., 1968, Atlas de galaxias australes. Obs. Astron. Univ. Nacional de Córdoba, Córdoba
Shapiro K. L., Cappellari M., de Zeeuw T., McDermid R. M., Gebhardt K., van den Bosch R. C. E., Statler T. S., 2006, MNRAS, 370, 559
Smith M. D. et al., 2019, MNRAS, 485, 4359
Stockmann M. et al., 2020, ApJ, 888, 4
Tahmasebzadeh B. et al., 2025, ApJ, 989, L42
Taylor M. A. et al., 2025, ApJ, 991, L24
Thater S. et al., 2022, MNRAS, 509, 5416
Thater S., Lyubenova M., Fahrion K., Martín-Navarro I., Jethwa P., Nguyen D. D., van de Ven G., 2023, A&A, 675, A18
Thatte N. A. et al., 2016, in Evans C. J., Simard L., Takami H., eds, Proc. SPIE Conf. Ser. Vol. 9908, Ground-based and Airborne Instrumentation for Astronomy VI. SPIE, Bellingham, p. 99081X
Thatte N. A. et al., 2020, in Evans C. J., Bryant J. J., Motohara K., eds, Proc. SPIE Conf. Ser. Vol. 11447, Ground-based and Airborne Instrumentation for Astronomy VIII. SPIE, Bellingham, p. 114471W
Tremaine S., Richstone D. O., Byun Y.-I., Dressler A., Faber S. M., Grillmair C., Kormendy J., Lauer T. R., 1994, AJ, 107, 634
van de Sande J. et al., 2013, ApJ, 771, 85
van den Bosch R. C. E., 2016, ApJ, 831, 134
van der Wel A. et al., 2014, ApJ, 788, 28
van der Wel A. et al., 2016, ApJS, 223, 29
van der Wel A. et al., 2021, ApJS, 256, 44
van Dokkum P. G. et al., 2009, Publ. Astron. Soc. Pac., 121, 2
Van Rossum G., Drake F. L., 2009, Python 3 Reference Manual. CreateSpace, Scotts Valley, CA
Verro K. et al., 2022, A&A, 660, A34
Virtanen P. et al., 2020, Nat. Methods, 17, 261
Voggel K. T. et al., 2018, ApJ, 858, 20
Walsh J. L., Barth A. J., Ho L. C., Sarzi M., 2013, ApJ, 770, 86
Walsh J. L., van den Bosch R. C. E., Gebhardt K., Yıldırım A., Richstone D. O., Gültekin K., Husemann B., 2016, ApJ, 817, 2
Whitaker K. E. et al., 2010, ApJ, 719, 1715
Williams R. J., Quadri R. F., Franx M., van Dokkum P., Labbé I., 2009, ApJ, 691, 1879
Wright E. L., 2006, PASP, 118, 1711
Zhu K. et al., 2025, ApJS, 280, 55
Zieleniewski S., Thatte N., Kendrew S., Houghton R. C. W., Swinbank A. M., Tecza M., Clarke F., Fusco T., 2015, MNRAS, 453, 3754

This paper has been typeset from a TEX/LATEX file prepared by the author.